Bihalogenated Thiophene-Based Terpolymers for High-Performance Semitransparent Organic Solar Cells Processed by an Eco-Friendly Solvent and Layer-by-Layer Deposition

Sung Jae Jeon, Nam Gyu Yang, Young Hoon Kim, Ji Hee Yun, and Doo Kyung Moon*

Read Online

ACCESS | 📊 Metrics & More | 📖 Article Recommendations | 🔵 Supporting Information

ABSTRACT: The development of photoactive materials simultaneously satisfying high performance, low cost, and eco-friendly processability remains challenging in organic solar cells (OSCs). Herein, a synergistic strategy is proposed to design three terpolymers (PM7(ClCl = 0.2), PM7(ClBr = 0.2), and PM7(BrBr = 0.2)) based on bihalogenated thiophenes with relatively low cost, for improving the optical and electrochemical properties, solubility in nontoxic solvents, and crystallinity and miscibility balance. In summary, a bulk-heterojunction (BHJ)-processed device based on PM7(ClCl = 0.2) with 20% dichlorinated thiophene achieves the highest power conversion efficiency (PCE) of 15.2% using toluene (best PCE ≈ 15.8% on the ternary blend). Moreover, high-performance semitransparent OSCs (ST-OSCs) were fabricated by a combination of layer-by-layer (LBL) and sequential dynamic and static spin-coating techniques according to the molecular weight of PM7(ClCl = 0.2). Using this unique LBL strategy, the PM7(ClCl = 0.2)-MW (H; high molecular weight)-processed ST-OSCs yield a high PCE of 11.5% and an average visible transmittance (AVT) of 27.1% with outstanding tolerance to device reproducibility. By optimizing ST-OSCs with tungsten trioxide as a distributed Bragg reflector, a light utilization efficiency (LUE) of 3.61% is realized with a PCE of 10.8% and an AVT of 33.4% (certified PCE ≈ 11.157%; LUE ≈ 3.73%). This study provides a novel perspective for designing and developing actual photoactive materials for OSC commercialization.

KEYWORDS: organic solar cells, bihalogens, eco-friendly solvents, layer-by-layer deposition, sequential dynamic and static spin-coating, semitransparent organic solar cells
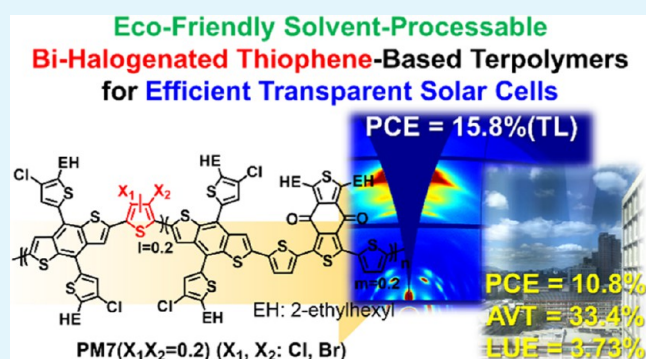
1. INTRODUCTION

Organic solar cells (OSCs) have attracted considerable research attention in both academic and industrial communities because of their unique characteristics, such as solution processability, intrinsic mechanical flexibility, lightweight, and environmental friendliness.[1] Since the innovative development of non-fullerene acceptors (NFAs) like Y6,[2] OSCs have broken through to a power conversion efficiency (PCEs) of over 18%, which is comparable to silicon and perovskite solar cells.[3−5] Furthermore, such high-performance OSCs can be more highlighted with advantages of semitransparency and vivid color for practical application to the distributed installment of roofs or windows.[6,7] In recent years, considerable efforts have been made in the development of semitransparent OSCs (ST-OSCs), and the PCE has reached 12.91% with an average visible transmittance (AVT) of 22.49% using a wide-band-gap polymer donor D18 with narrow absorption as a smart strategy for decreasing the D18 weight ratio and decreasing the D18 layer thickness.[6,7] This progress for ST-OSCs was achieved based on many studies such as the ternary strategy, decreasing the content of the wide-band-gap polymer donor, and

adjusting the active layer thickness.[8−12] Nevertheless, OSCs still have many problems to solve in the aspect of cost,[13−16] stability,[17,18] and processability[4,19,20] Over the last few years, a great deal of OSC research studies has focused on the development of materials and device architectures for high-performance individual components.[1,5,21] However, there remains a need for codesign and integrated approaches between components to achieve efficient power systems optimized for specific OSC applications.[19]

To solve the issue, high-processability donor polymers should be developed as they have the potential for efficiency and cost and facilitate customization of the components. Although highly efficient photovoltaic performances have been
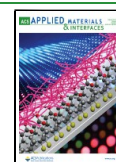
achieved using superior Y6 derivatives, most donor polymers are strongly dependent on processing in toxic solvents, such as chloroform (CF) and chlorobenzene (CB), because of their solubility limit;[3,4,21,22] this hinders scalable fabrication and industrial printability. Furthermore, considering the large-scale production requirement of large-area OSC modules, donor polymers must be as inexpensive as possible.[13–15] Among the donor polymers with a PCE beyond 15%, only a few polymers were designed to have low synthetic complexity, which can be synthesized from widely available raw materials and with relatively fewer synthetic steps.[15,16]

In polymer building blocks, the regio-regularity between the donor (D) and acceptor (A) moieties is critical for achieving high-performance polymers with strong interchain packing and well-ordered crystallinity.[23,24] However, these polymers are sometimes difficult to dissolve in eco-friendly solvents such as toluene (TL) and o-xylene (XY) due to excessive aggregation. Terpolymer strategies of the type $D_1–A_1–D_1–A_2$ or $D_1–A_1–D_2–A_1$ can be a simple solution by endowing a small regio-random segment into the main D–A polymer backbone.[19,25,26] According to the literature, many terpolymers exhibited high solubility and efficiency in nontoxic solvents, which were proved by measuring the stability.[19,20,27] Although fluorination of the polymers can increase the synthetic complexity, it is an effective method of finely tuning the frontier energy levels and other physiochemical properties.[28,29] Thus, the fluorinated donor polymers generally exhibit superior device performances because of their lower highest occupied molecular orbital (HOMO) levels, planar backbones, and higher internal dipole moments than their unsubstituted counterparts.[28,29] To achieve similar effects as in fluorination, cost-effective chlorination could be considered a reasonable alternative. Furthermore, the chlorine (Cl) atom exhibits a larger atomic size than the fluorine (F) atom, which can enhance the crystalline properties and intermolecular packing, which generates better PCE.[14,30] However, chlorination should be paid more attention to as it may offer a negative effect because of its large steric hindrance when introduced in the main conjugated backbone.[31–33]

In this study, we newly designed and synthesized three terpolymers, namely, PM7(ClCl = 0.2), PM7(ClBr = 0.2), and PM7(BrBr = 0.2), based on the main polymer backbone of PM7 with a relatively low synthetic complexity for enhancing performance and processability. Especially, bihalogenated thiophenes, such as dichloro/chlorobromo/dibromo-thiophene (ClCl/ClBr/BrBr), were incorporated with a 20% concentration as the third building block of the type $D_1–A_1–D_1–A_2$ into PM7. Each bihalogenated thiophene obtained by easy synthetic routes can cause slight tilting of the polymer curvature and enable the modulation of the structural flexibility and solubility of PM7. Furthermore, its two large halogen atoms can efficiently increase the dipole moments and decrease HOMO levels compared with F. More importantly, bihalogen effects on the main conjugated polymer backbone can be achieved by balancing the crystallinity and miscibility without a complicated design.

Consequently, we achieved a high PCE of 15.2% with a bulk-heterojunction (BHJ) of PM7(ClCl = 0.2) and BTP-eC9 using a dynamic spin-coating (DS) and TL solvent among the three terpolymers. To enhance the long-range regularity in the edge-on orientation, we introduced P(SBDT-ClCl) as a third component in the PM7(ClCl = 0.2):BTP-eC9 blend, which resulted in the best performance with 15.8%. Furthermore,

highly efficient ST-OSCs were fabricated using a combination of layer-by-layer (LBL) and sequential dynamic and static spin-coating (DSS) techniques inspired by the UV–Vis results from spin-coating CF onto neat films of PM7(ClCl = 0.2) according to the molecular weight (MW) (moderate/high/very high, M/H/VH). The optimized ST-OSCs yield a high PCE of 11.5% with an average visible transmittance (AVT, @ 380–780 nm) of 27.1% at PM7-MW(H) with outstanding tolerance to device reproducibility. By optimizing the ST-OSCs with tungsten trioxide (WO_3) as a distributed Bragg reflector (DBR), a light utilization efficiency (LUE) of 3.61% was realized with a PCE of 10.8% and an AVT of 33.4%. Moreover, this device was encapsulated and sent to the Nano Convergence Practical Application Center (NCPAC) in Korea for certification, which revealed that it had a PCE of 11.157% and LUE of 3.73%. The high-performing and eco-friendly solvent-processable terpolymers based on bihalogenated thiophenes, and their highly transparent device design strategies have demonstrated the potential for a significant impact on the industrialization of OSCs.

2. RESULTS AND DISCUSSION

2.1. Preceding Study: Bihalogenated Thiophene-Based D−A Polymers.
In this section, three D−A polymers, namely, P(ClCl), P(ClBr), and P(BrBr), based on bihalogenated thiophenes were synthesized as a precedent study, and their synthetic details are described in the Supporting Information (Figures S1−S7). Notably, bihalogenated thiophenes were obtained with a low synthetic complexity compared with other A units.[16,34] All D−A polymers effectively formed a wide band gap (E_g) of 1.9 eV or more, and a deeply-lying HOMO level of −5.6 eV or less using the 2DBDT structure without any halogen substituents as a D unit (Figures S8 and S9). However, the introduction of Cl and Br atoms, which can result in larger torsion angles to the main conjugated backbone than the F atoms, resulted in low crystallinity of all of the three polymers (Figures S10 and S11). As displayed in the UV−Vis spectra in the solution and film states, the prominence of the 0−0 peak was in the order P(BrBr), P(ClBr), and P(ClCl). P(ClCl) exhibited the most substantial aggregation among the three polymers. Furthermore, the two-dimensional grazing-incidence wide-angle X-ray scattering (2D-GIWAXS) patterns in the out-of-plane (OOP) direction revealed that P(ClCl) exhibited the closest lamellar crystalline structure and π−π stacking distance among the three polymers. By contrast, P(ClBr) exhibited the farthest π−π stacking distance because of the asymmetric structure and high regio-randomness. P(BrBr) had the farthest lamellar distance because of the Br atom, which was the largest among the halides and caused considerable tilting on both sides adjacent to 2DBDT. Finally, all D−A polymers mixed with face-on-dominant Y6 acceptors exhibited PCEs in the order P(ClCl), P(ClBr), and P(BrBr) in each optimized device according to their trend in crystallinity (Figure S12). The photovoltaic performances revealed a close correlation with the trend of crystallinity mentioned earlier. Tables S1−S4 summarize the details of all parameters.

2.2. Bihalogenated Thiophene-Based Terpolymers: Design Concept, Physical and Thermal Properties, and Theoretical Calculations.
Given the results of the precedent study, we designed and synthesized terpolymers by introducing bihalogenated thiophenes with a 20% concentration as a third component instead of the BDD unit in the main backbone of

PM7 consisting of benzodithiophenedione (BDD) and Cl-substituted two-dimensional benzodithiophene (Cl-2DBDT) (Figures S13−S15). The synthetic details of PM7(ClCl = 0.2), PM7(ClBr = 0.2), and PM7(BrBr = 0.2) are summarized in Scheme 1, and the procedures are described at the end of the

Scheme 1. Synthetic Routes of Bihalogenated Thiophene-Based Terpolymers: PM7(ClCl = 0.2), PM7(ClBr = 0.2), and PM7(BrBr = 0.2)
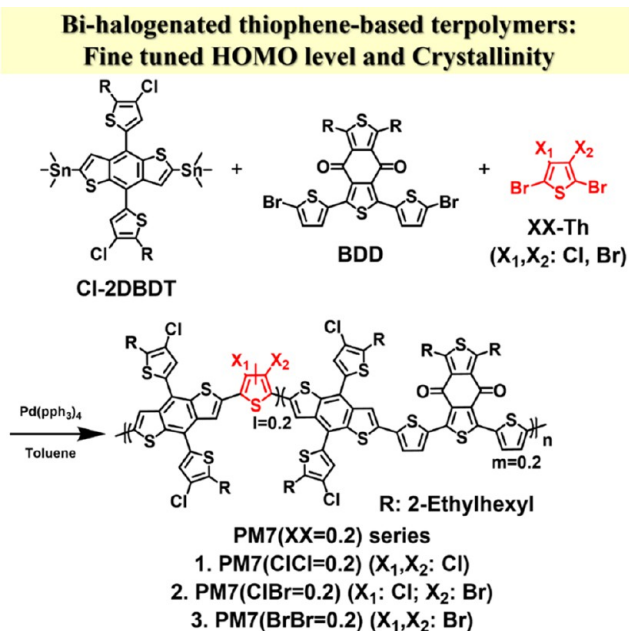
study. This terpolymer strategy based on Cl-2DBDT is obtained with a relatively low cost compared with F-substituted 2DBDT (F-2DBDT). This strategy is a simple and cost-effective method for improving the optical and electrochemical properties, solubility, and crystallinity of terpolymers to realize high photovoltaic performances.[30,35] All terpolymers were successfully synthesized with high yields of more than 85% and exhibited excellent solubility in both halogenated (CF and CB) and nonhalogenated (TL and XL) solvents. Introducing the large-size bihalogen atoms into the polymer backbone gradually decreased the number-average molecular weights (M_n) and broadened polydispersity indices (PDI). The results of thermogravimetric analyses confirmed that the decomposition temperature (T_d; the temperature at which 5% sample weight loss occurred) for each polymer was more than 400 °C, which is derived from the number of many rigid halogen substituents (Figure S16).[36] Furthermore, differential scanning calorimetry analysis revealed no obvious thermal transitions, except a glass transition between 30 and 300 °C (Figure S17). Details of the physical and thermal properties of terpolymers are summarized in Table 1.

We performed density functional theory (DFT) calculations on the B3LYP/6-31G(d,p) basis set using Gaussian 09 to investigate the influences of the bihalogenated thiophene moieties on the chemical geometry and frontier molecular energy levels of the PM7 polymer backbone (Figures S18 and S19). For computational purposes, we focused on terpolymers with 50% concentrations of each bihalogenated thiophene at 2 repeating units (n = 2).[20] The results of the DFT calculations are summarized in Table S5. The optimized geometries of the bihalogenated thiophene-based model compounds and PM7

Table 1. Physical and Thermal Properties of Bihalogenated Thiophene-Based Terpolymers

terpolymer	yield [%]	M_n^a [kDa]	M_w^a [kDa]	PDI^a	T_d^b [°C]
PM7(ClCl = 0.2)	91.0	28.9	36.2	1.25	435
PM7(ClBr = 0.2)	87.5	25.5	43.8	1.72	422
PM7(BrBr = 0.2)	85.0	21.7	59.7	2.75	417

^{a}Parameters (M_n: number-average molecular weight; M_w: weight-average molecular weight; PDI: polydispersity index) determined by GPC in chloroform using polystyrene standards. ^{b}Temperature corresponding to 5% weight loss.

dimers exhibited distinct different curvatures (Figure S18). Among the bihalogenated thiophene-based model compounds with PM7(ClCl = 0.2), dihedral angles (θ_1, θ_2, θ_3, θ_4, θ_5, θ_6, and θ_7) between each motif were −9.23, −21.55, 24.02, 18.59, −14.36, −15.67, and 17.64° and −34.16, 10.19, 13.13, 15.33, and 16.85° for PM7 and PM7(ClCl = 0.2), respectively. Therefore, PM7(ClCl = 0.2) likely exhibits lower planarity than PM7. However, the back angle between the dichlorinated thiophene and adjacent Cl-2DBDT motif was 34.16° on one side, which revealed a large torsion, whereas a slight tilting angle (10.19°) was observed on the other side. A similar trend was observed in all bihalogenated thiophene models. Therefore, bihalogenated thiophene-based terpolymers can be planar with a zig-zag structure, which revealed a strong intermolecular packing order, unlike PM7, which had a linear structure, as displayed in each side view. Furthermore, the dibrominated thiophene-based terpolymer with big atoms exhibited the most planar structures among the model compounds, which contradicts the expected structure. This outcome can be attributed to the steric hindrance with the adjacent Cl-2DBDT motif that was minimized for C−Br because the C−Br bond length at 1.887 Å was longer than that of C−Cl at 1.735 Å. Thus, PM7(BrBr = 0.2) was expected to exhibit the strongest intermolecular aggregation among bihalogenated thiophene-based terpolymers. The molecular energy levels with orbital distributions of HOMO and the lowest unoccupied molecular orbital (LUMO) and their electrostatic potential (ESP) surfaces are directly related to the bihalogenated thiophenes, as shown in Figure S19. The results revealed that introducing bihalogenated thiophenes results in effectively downshifted HOMO energy levels and slightly upshifted LUMO energy levels, which results in enlarged band gaps. Compared with PM7, deeper HOMO energy levels of terpolymers can result in higher open-circuit voltage (V_{oc}) values in the corresponding OSCs. All terpolymers exhibit continuous negative ESP across most of the conjugated backbone similar to PM7, which are favorable for charge carrier transport when interacting with positive Y6 derivatives.[16,37] Finally, the net dipole moments of all terpolymers were higher with over twice that of PM7, which can improve the charge separation in the network between the donor and acceptor.[37]

2.3. Optical and Electrochemical Properties. UV−Vis spectroscopy and cyclic voltammetry (CV) were performed to investigate the optical and electrochemical properties of terpolymers. From solutions to thin films, all terpolymers exhibited red shifts in two absorption bands at ∼350 and 500−650 nm, which correspond to the π−π* transition and intramolecular charge transfer, respectively.[20,25] As displayed in Figure 1a, the molar absorption coefficients (ε) were calculated using the Beer−Lambert equation from the averaged UV−Vis
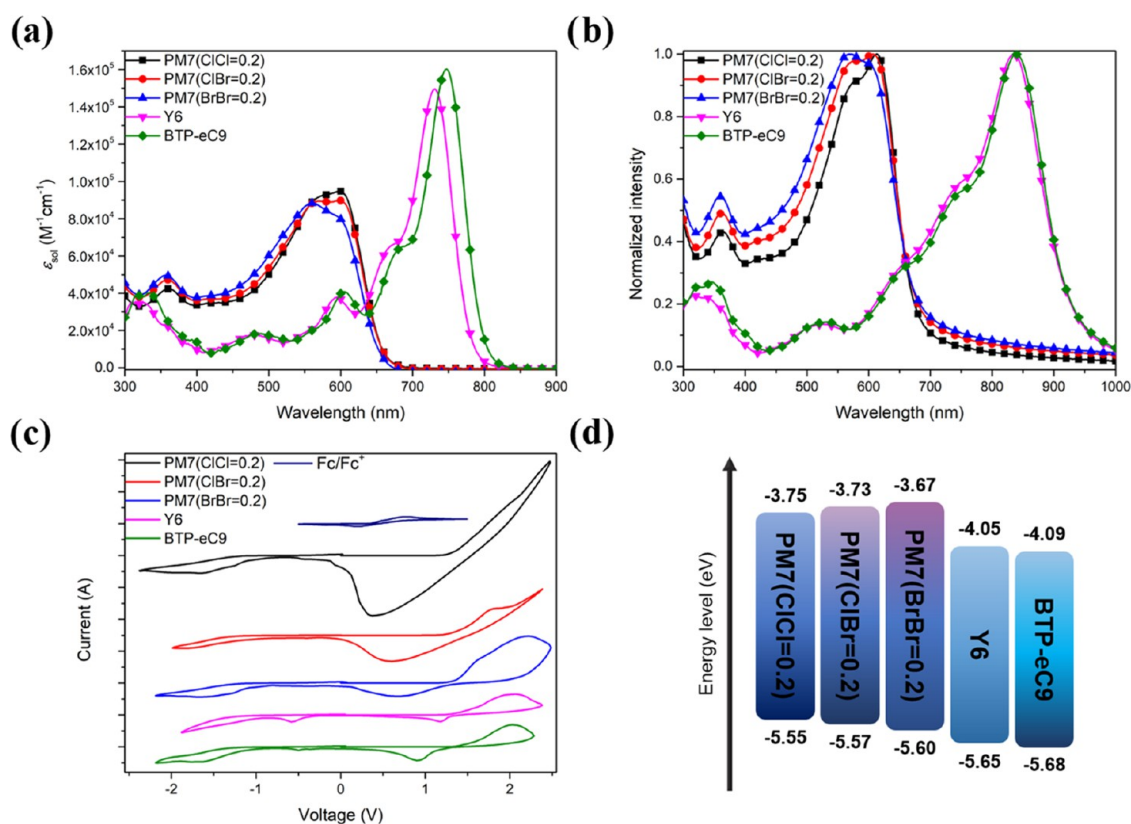
Figure 1. UV−Vis absorption spectra, CV curves, and energy-level band diagram of bihalogenated thiophene-based terpolymers and Y6 derivatives: (a) average molar absorption coefficients in chloroform (measured using 10^{-5} M chloroform solutions), (b) normalized absorption spectra in thin films, (c) CV curves of thin films, and (d) energy-level band diagram.

Table 2. Optical and Electrochemical Properties of Bihalogenated Thiophene-Based Terpolymers

	UV−Vis			CV				
terpolymer	λ_{max}^{solu} [nm]	ε [M^{-1} cm^{-1}] (λ_{max} [nm])	λ_{max}^{film} [nm]	$E_g^{opt\,a}$ [eV]	E_{ox}^{onset} [V]	$E_{HOMO}{}^{b}$ [eV]	E_{red}^{onset} [V]	$E_{LUMO}{}^{b}$ [eV]
PM7(ClCl = 0.2)	361, 581, 599	42 395 (361), 94 777 (599)	364, 613	1.83	1.24	−5.55	−0.56	−3.75
PM7(ClBr = 0.2)	359, 569, 598	47 139 (359), 89 767 (598)	362, 581, 607	1.84	1.26	−5.57	−0.58	−3.73
PM7(BrBr = 0.2)	356, 561	49 628 (356), 88 309 (561)	360, 568	1.85	1.29	−5.60	−0.64	−3.67

$^{a}\lambda_{onset}$ is calculated from the intersection of the tangent on the low energetic edge of the absorption spectrum with the baseline, $E_g^{opt} = \frac{1240}{\lambda_{onset}}$.
$^{b}E_{HOMO} = -4.8[E_{ox}^{onset}$ (vs Ag/AgCl) $- E_{1/2}(Fc/Fc^+$ vs Ag/AgCl)] and $E_{LUMO} = -4.8[E_{red}^{onset}$ (vs Ag/AgCl) $- E_{1/2}(Fc/Fc^+$ vs Ag/AgCl)], where $E_{1/2}(Fc/Fc^+$ vs Ag/AgCl) is 0.49 eV.

data measured in chloroform solutions with various concentrations on the order of 10^{-5} M.[14,20,31] The maximum ε values for PM7(ClCl = 0.2) and PM7(ClBr = 0.2) were 9.48×10^4 and 8.98×10^4 M^{-1} cm^{-1} at each 0−0 peak, whereas PM7(BrBr = 0.2) exhibited 8.83×10^4 at 0−1 peak. Especially, it can be seen that PM7(BrBr = 0.2) exhibited no 0−0 peak in both solution and film states, whereas PM7(ClBr = 0.2) exhibited a medium shoulder peak and PM7(ClCl = 0.2) exhibited a pronounced shoulder peak, which indicated gradually increased J-aggregates and decreased H-aggregates with the same tendency of bihalogenated thiophene-based D−A polymers.[38,39] Based on their absorption onsets in the thin-film state, PM7(ClCl = 0.2), PM7(ClBr = 0.2), and PM7(BrBr = 0.2) exhibited wide optical band gaps (E_g^{opt}) of 1.83, 1.84, and 1.85 eV, respectively (see Figure 1b). Among the terpolymers, PM7(ClCl = 0.2) exhibited a highly lamellar crystalline structure with a 14 nm red-shifted shoulder peak in the film state. These trends are consistent with UV data using toluene (TL) (Figure S20). In addition, this effect resulted in

an enhancing complementary absorption with Y6 derivatives, such as Y6[2] and BTP-eC9[4], which exhibit a strong absorption band in the range of 700−900 nm. Next, the energy levels of the three terpolymers were estimated through CV. As displayed in Figure 1c, the HOMO and LUMO levels of PM7(ClCl = 0.2), PM7(ClBr = 0.2), and PM7(BrBr = 0.2) were calculated to be −5.55/−3.75, −5.57/−3.73, and −5.60/−3.67 eV, respectively, which indicates that the introduction of halogen atoms with a large atomic size downshifted the HOMO level and simultaneously upshifted the LUMO level.[35,36] This trend differed slightly from the result of the DFT calculation, which may have originated from the increased steric hindrance effect on the polymer backbone. As a result, these terpolymers matched well with the energy levels of the Y6 derivatives such as Y6 and BTP-eC9.[2,4] As displayed in Figure 1d, the energy levels are well-aligned with acceptors, and the values of V_{oc} for terpolymers theoretically increased in the order PM7(ClCl = 0.2), PM7(ClBr = 0.2), and PM7(BrBr = 0.2). Furthermore, all terpolymers exhibited

Table 3. Photovoltaic Performance of the Optimized Devices with a Conventional Structure of Bihalogenated Thiophene-Based Terpolymer Blends and Ternary Blends

active layer[a]	V_{oc} [V]	J_{sc} [mA cm^{-2}]	FF [%]	PCE$_{max}$/PCE$_{ave}$[b] [%]	E_{loss}[c] [eV]
PM7(ClCl = 0.2):Y6 = 1.0:1.0	0.865	24.19	70.02	14.7/14.5 ± 0.16	0.462
PM7(ClBr = 0.2):Y6 = 1.0:1.0	0.879	24.45	65.39	14.1/13.8 ± 0.26	0.456
PM7(BrBr = 0.2):Y6 = 1.0:1.0	0.899	22.76	62.21	12.7/12.5 ± 0.20	0.423
PM7(ClCl = 0.2):BTP-eC9 = 1.0:1.0	0.879	24.21	71.63	15.2/15.1 ± 0.14	0.440
PM7(ClCl = 0.2):PC$_{71}$BM:BTP-eC9 = 1.0:0.1:0.9	0.899	22.38	72.52	14.6/14.4 ± 0.19	0.422
PM7(ClCl = 0.2):P(SBDT-ClCl):BTP-eC9 = 0.9:0.1:1.0	0.879	24.70	72.57	15.8/15.5 ± 0.25	0.459

[a]Postannealing at 100 °C for 10 min. [b]Average PCE values calculated from 10 independent cells. [c]Energy loss (E_{loss}) calculated from the equation of $E_{loss} = E_g^{op} - eV_{oc}$.
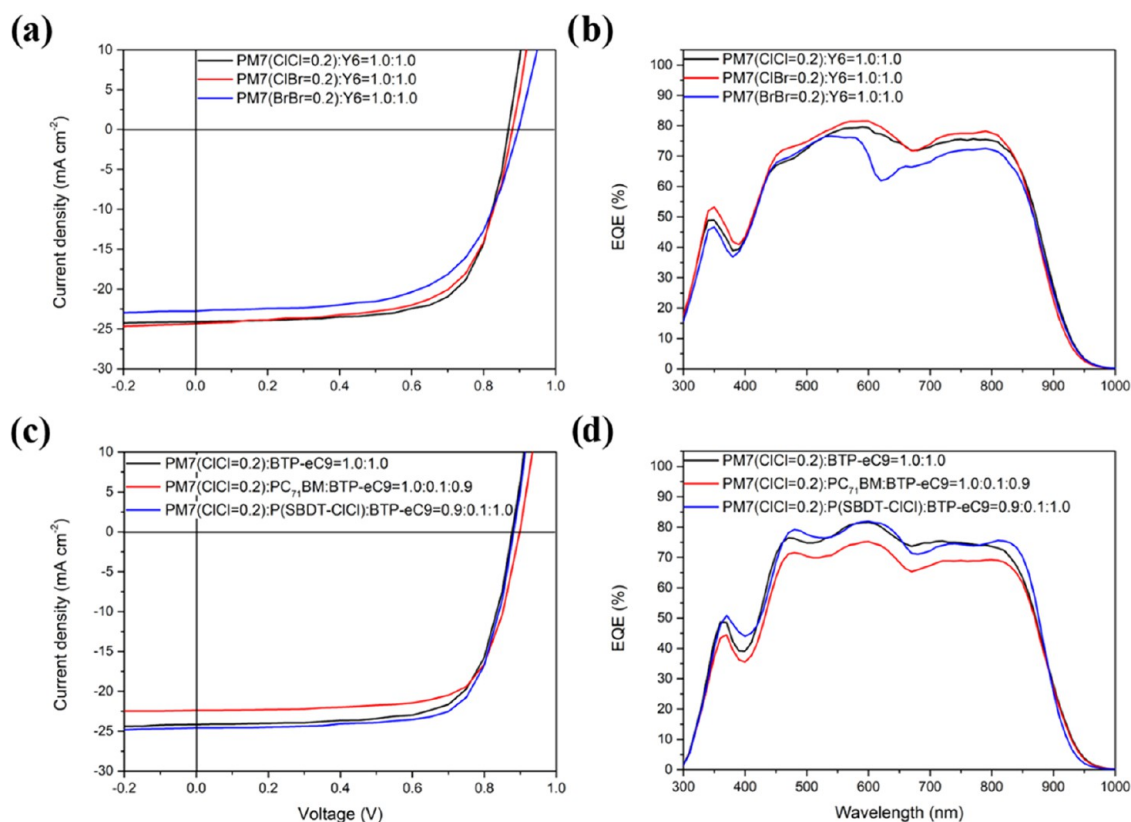

Figure 2. (a, c) $J-V$ and (b, d) external quantum efficiency (EQE) curves of the optimized devices with the conventional structure of bihalogenated thiophene-based terpolymer and ternary blends.

minimized HOMO offsets under ~0.10 eV with Y6 derivatives, which can be attributed to efficient charge transfer in photovoltaic devices.[40,41] The results are summarized in Table 2.

2.4. Photovoltaic Performance. To investigate the photovoltaic performances of the three terpolymers, all devices were fabricated and optimized with a conventional structure (ITO/PEDOT:PSS/polymer:NFA/PDINN/Ag). The detailed fabrication process and various optimized conditions for the devices are displayed in the Supporting Information (Tables S6−S9). The photovoltaic parameters for the optimized terpolymer blends are summarized in Table 3. First, we selected Y6 as an acceptor with a light-harvesting capability in the visible to near-infrared (NIR) regions, and well-matched energy-level alignments.[2] In short, all Y6-based devices for terpolymers with high solubility in eco-friendly solvents, such as TL and XY, exhibited higher efficiencies than those of CF and CB. As displayed in Figure 2a, with a decreased HOMO level of terpolymers, V_{oc}s of PM7(ClCl = 0.2), PM7(ClBr =

0.2), and PM7(BrBr = 0.2) gradually increased with the V_{oc} of 0.865, 0.879, and 0.899 V. Despite the low V_{oc}, the PM7(ClCl = 0.2):Y6-based device exhibited the highest PCE of 14.7%, which resulted in a reasonable short-circuit current density (J_{sc}) and FF over 70%. By contrast, the PM7(ClBr = 0.2):Y6 and PM7(BrBr = 0.2):Y6-based devices exhibited slightly low PCEs of 14.1 and 12.7%, respectively. In particular, this result for terpolymers with the main polymer backbone of PM7 is critical because of their potential to be used as eco-friendly solvents for fabricating high-efficiency Y6-based OSC devices. Figure 2b displays the external quantum efficiency (EQE) spectra of the Y6-based devices based on the three terpolymers. All of the devices exhibited a broad photoresponse in the range of 300−900 nm, which indicated their effective light-harvesting ability. The calculated integrated current density values are consistent with those from the $J-V$ curves, with a mismatch of <5%. The PM7(ClCl = 0.2) and PM7(ClBr = 0.2)-based devices exhibited higher EQEs with over 75% in the region 550−850 nm, whereas the PM7(BrBr =

0.2) device exhibited a lower EQE value because of the depressed J-aggregates and lamellar crystallinity resulting in low J_{sc}.

To enhance the device performance of PM7(ClCl = 0.2), we fabricated binary and ternary devices based on the BTP-eC9 acceptor with a higher crystallinity and processability comparison with Y6.[4] First, the PM7(ClCl = 0.2):BTP-eC9 device of the binary blend structure exhibited a higher PCE of 15.2% with a slight increase in each parameter compared with those of PM7(ClCl = 0.2):Y6. Next, we introduced PC$_{71}$BM as a third component into PM7(ClCl = 0.2):BTP-eC9 to enhance the optical response, phase separation, and V_{oc},[42,43] but achieved poor efficiency with a PCE of 14.6%. To increase the PCE of the PM7(ClCl = 0.2)-based device, we synthesized a novel polymer, P(SBDT-ClCl) with a long-range order crystalline property and well-matched energy level, and subsequently introduced the PM7(ClCl = 0.2):BTP-eC9 blend film as the third component.[44] The characterization of P(SBDT-ClCl) was systematically studied and is depicted in the Supporting Information (Figures S21−S27 and Tables S10−S13). Although P(SBDT-ClCl):BTP-eC9 exhibited a PCE of 12.2% in the binary blend, the PM7(ClCl = 0.2):P(SBDT-ClCl):BTP-eC9-ternary device reached the best performance of 15.8% because of simultaneously enhanced J_{sc} and FF values. To the best of our knowledge, PM7(ClCl = 0.2) with a relatively low cost exhibits one of the highest performances using an eco-friendly solvent for the Y6 derivative-based devices reported so far.[35−47] The $J−V$ and EQE curves are depicted in Figure 2c,d.

This efficiency trend may result from the optimal HOMO offset difference between the donor and acceptor units, and the minimized energy loss (E_{loss}), which increases the probability of charge carrier separation.[40,41] Generally, the E_{loss} of OSCs is determined by both the competition between charge transport/extraction and recombination as well as the driving force of exciton dissociation.[48,49] Therefore, E_{loss} is a critical parameter in the evaluation of photovoltaic performance. This parameter can be estimated through $E_{loss} = E_g^{opt} - eV_{oc}$, where E_g^{opt} is the lowest optical band gap among the donor and acceptor, and e is the elementary charge. Among methods to determine E_g^{opt}, we selected a widely accepted method in which E_g^{opt} is deduced from the onset EQE curves. The E_{loss} values of all of the devices are summarized in Table 3. First, E_{loss} for PM7(ClCl = 0.2), PM7(ClBr = 0.2), and PM7(BrBr = 0.2) decreased with 0.462, 0.456, and 0.423 eV, respectively, because the HOMO offset was gradually minimized. Although PM7(ClCl = 0.2) exhibited the highest E_{loss} among the Y6-based OSCs, it exhibited the best efficiency, which could be attributed to efficient charge carrier separation derived from the highest dipole moment of the polymer.[37] By introducing BTP-eC9 instead of Y6, the PM7(ClCl = 0.2)-based device exhibited a higher efficiency with a lower E_{loss} of 0.440 eV; additionally, by incorporating PC$_{71}$BM into the PM7(ClCl = 0.2):BTP-eC9 blend, E_{loss} was minimized to 0.422 eV, which is lower than that of most high-performance OSCs. Despite the incredibly lowest E_{loss}, the PM7(ClCl = 0.2):PC$_{71}$BM:BTP-eC9-based device exhibited lower PCE than PM7(ClCl = 0.2):BTP-eC9 did, which may have originated from the limited crystallinity according to the increased amorphous phase of PC$_{71}$BM.[44] By contrast, the incorporation of P(SBDT-ClCl) in the PM7(ClCl = 0.2):BTP-eC9 blend revealed a larger E_{loss} of 0.440 eV than that of the PC$_{71}$BM-based ternary device. Nevertheless, the highest PCE was achieved in this ternary

device, which indicates that P(SBDT-ClCl) may be beneficial for high crystallinity.[44]

2.5. Charge Transport Analysis. To investigate the contribution to device performance between the donor and acceptor in active layers, photoluminescence (PL) measurements were conducted on each film of the pristine donor and acceptor and optimized terpolymer blends.[20,32,36,48,49] All pristine and blended films exhibited a pronounced PL emission peak in the ranges 600−900 and 850−1400 nm when excited at 550 and 820 nm, respectively. The PL spectra are presented in Figure S28. The PL quenching (PLQ) rates and frontier energy-level offsets are summarized in Table S14. All of the donor to the blend (D → B) and acceptor to the blend (A → B) PLQ rates were investigated under the excitation wavelengths at 550 and 820 nm and showed PLQ$_{D \to B}$ and PLQ$_{A \to B}$, respectively. First, for the bihalogenated thiophene-based terpolymer and Y6 blends, the PLQ values were gradually decreased in both PLQ$_{D \to B}$ and PLQ$_{A \to B}$ with an order of PM7(ClCl = 0.2):Y6, PM7(ClBr = 0.2):Y6, and PM7(BrBr = 0.2):Y6 blend films, which is consistent with the J_{sc} trend of the devices. In this case, the PM7(BrBr = 0.2)-based film despite having a minimized HOMO offset revealed that the photoexcited charge carriers were insufficiently transferred between the constituent materials. This result implied not only charge transfer dynamics but also other problems such as morphology and crystallinity.[44] Next, although a slightly increased energy offset exists between the donor and acceptor, the PM7(ClCl = 0.2):BTP-eC9 blend film showed higher quenching efficiencies in both PLQ$_{D \to B}$ and PLQ$_{A \to B}$ compared with that of PM7(ClCl = 0.2):Y6, which partially accounted for the improved J_{sc} value in the device. Finally, the PL emissions of PM7(ClCl = 0.2):PC$_{71}$BM:BTP-eC9 and PM7(ClCl = 0.2):P(SBDT-ClCl):BTP-eC9 ternary blend films exhibited obvious evidence of energy transfer according to the cascade energy-level alignment between the main components and each third component. Thus, a small amount of P(SBDT-ClCl) incorporated on the PM7(ClCl = 0.2):BTP-eC9 blend resulted in a remarkable difference in PLQ values compared with that of PM7(ClCl = 0.2):PC$_{71}$BM:BTP-eC9.[49] Thus, P(SBDT-ClCl) was conducted as the role of minimized energy offsets and highly efficient exciton dissociation in the ternary blend structure.[49] Therefore, the PM7(ClCl = 0.2):P(SBDT-ClCl):BTP-eC9 ternary blend film reached the best PLQ values with PLQ$_{D \to B}$ of 90.94% and PLQ$_{A \to B}$ of 92.68% among the fabricated devices.

The charge mobilities of PM7(ClCl = 0.2):Y6, PM7(ClBr = 0.2):Y6, PM7(BrBr = 0.2):Y6, PM7(ClCl = 0.2):BTP-eC9, PM7(ClCl = 0.2):PC$_{71}$BM:BTP-eC9, and PM7(ClCl = 0.2):P(SBDT-ClCl):BTP-eC9 blends were measured using the space−charge-limited current (SCLC) characteristics of electron-only and hole-only devices to verify the charge transport properties in each optimized device (Figure S29).[14,20,31] The details of SCLC measurements are summarized in the Supporting Information. The electron and hole mobilities (μ_e and μ_h) and their balance ratio (μ_e/μ_h) were calculated using the modified Mott−Gurney equation and are summarized in Table S15. Among the bihalogenated thiophene-based terpolymer and Y6 blends, PM7(ClCl = 0.2):Y6 exhibited the highest μ_e (5.57×10^{-4} cm^2 V^{-1} s^{-1}) and μ_h (3.15×10^{-4} cm^2 V^{-1} s^{-1}) with balanced mobilities (μ_e/μ_h: 1.77). By introducing BTP-eC9 instead of Y6 on PM7(ClCl = 0.2), the μ_e and μ_h of the PM7(ClCl = 0.2):BTP-eC9 blend
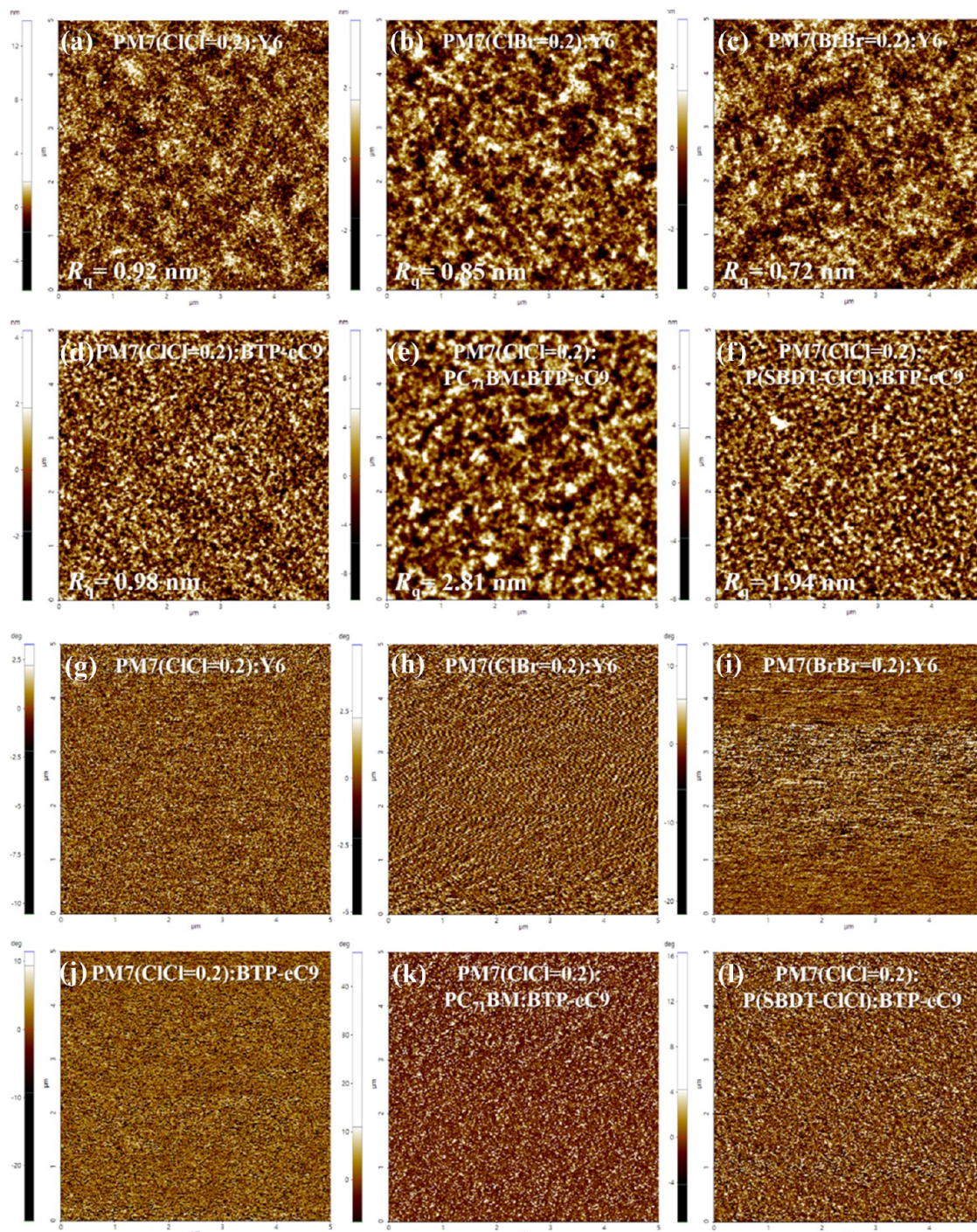
Figure 3. (a−f) AFM height and (g−l) phase images (5 μm × 5 μm) of the optimized bihalogenated thiophene-based terpolymer blends and ternary blends: (a, g) PM7(ClCl = 0.2):Y6, (b, h) PM7(ClBr = 0.2):Y6, (c, i) PM7(BrBr = 0.2):Y6, (d, j) PM7(ClCl = 0.2):BTP-eC9, (e, k) PM7(ClCl = 0.2):PC$_{71}$BM:BTP-eC9, and (f, l) PM7(ClCl = 0.2):P(SBDT-ClCl):BTP-eC9.

were enhanced to 6.42×10^{-4} and 6.01×10^{-4} cm^2 V^{-1} s^{-1}, respectively. The electron/hole mobility ratio was 1.66, which is consistent with the increased FF of the device.[22,36,38,41] For a ternary blend device incorporated with PC$_{71}$BM on PM7(ClCl = 0.2):BTP-eC9, its μ_e and μ_h were decreased by ∼2 times than those of the PM7(ClCl = 0.2):BTP-eC9 binary blend. Furthermore, its μ_e/μ_h was 0.85, which resulted in a higher FF of 72.52%. Despite the increased V_{oc} and FF, PM7(ClCl = 0.2):PC$_{71}$BM:BTP-eC9-based device exhibited a lower PCE than that of PM7(ClCl = 0.2):BTP-eC9 because of the

decreased J_{sc}. However, the ternary blend for PM7(ClCl = 0.2):P(SBDT-ClCl):BTP-eC9 exhibited the highest μ_e (6.93×10^{-4} cm^2 V^{-1} s^{-1}) and μ_h (7.55×10^{-4} cm^2 V^{-1} s^{-1}) with a balanced mobility ratio of 0.92, which explained the simultaneously improved J_{sc} and FF derived from efficient charge transport and collection.[35,41] All data for SCLC is consistent with the former analysis results.

2.6. Morphological Analysis. To analyze the origin of photovoltaic performance differences for the fabricated devices, we investigated the surface morphologies of each
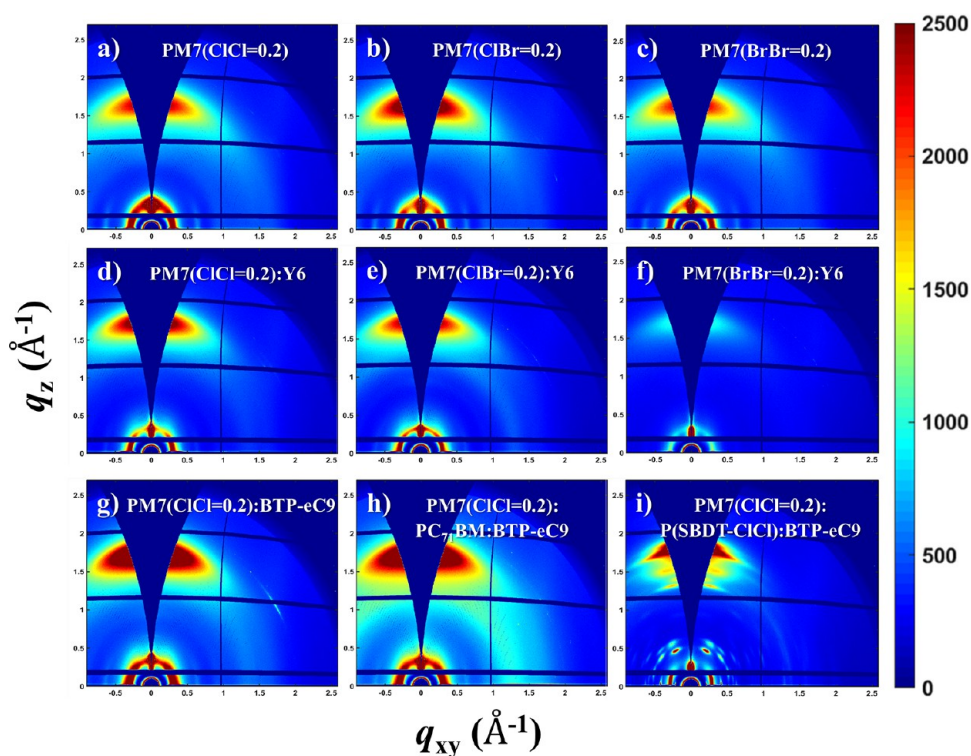
Figure 4. 2D-GIWAXS diffraction patterns of the neat terpolymer, optimized terpolymer blend, and ternary blend films: (a) PM7(ClCl = 0.2), (b) PM7(ClBr = 0.2), (c) PM7(BrBr = 0.2), (d) PM7(ClCl = 0.2):Y6, (e) PM7(ClBr = 0.2):Y6, (f) PM7(BrBr = 0.2):Y6, (g) PM7(ClCl = 0.2):BTP-eC9, (h) PM7(ClCl = 0.2):PC$_{71}$BM:BTP-eC9, and (i) PM7(ClCl = 0.2):P(SBDT-ClCl):BTP-eC9.

blend film through atomic force microscopy (AFM), as displayed in Figure 3.[4,14,20,26,31,50−53] The blend films were prepared under the same conditions as the optimized devices. According to AFM height images in Figure 3a−c, for the bihalogenated thiophene-based terpolymer and Y6 blends, the root-mean-square (R_q) roughness of PM7(ClCl = 0.2):Y6, PM7(ClBr = 0.2):Y6, and PM7(BrBr = 0.2):Y6 blend films were 0.92, 0.85, and 0.72 nm, respectively, which decreased with the decrement of steric hindrance estimated from DFT calculation. At the film surface, the topographies of the films gradually changed from a uniform into an aggregated morphology. According to the phase images (Figure 3g−i), the domain sizes of the blend films increased in the same sequence, which decreased the donor and acceptor interface and increased charge carrier recombination. Next, the PM7(ClCl = 0.2)-based blend film introduced BTP-eC9 instead of Y6, which resulted in more bicontinuous phase separation with appropriate domain sizes and an R_q of 0.98 nm, which facilitated charge transport for the least charge recombination, which afforded a higher FF.[4,20,52] This result can be more obviously seen through the comparison of the phase images in Figure 3g,j. For a ternary blend film incorporated with PC$_{71}$BM on PM7(ClCl = 0.2):BTP-eC9 as shown in Figure 3e, the AFM height image indicates a rough morphology and large-size aggregation with an R_q of 2.81 nm, which reveals poor charge transport and results in decreased J_{sc}.[52,53] By contrast, the other ternary combination, PM7(ClCl = 0.2):P(SBDT-ClCl):BTP-eC9-based blend film exhibited smooth and uniform features (Figure 3f,l). Likewise, a smooth active layer surface can have better contact with the top electron transport layer and electrode, which are beneficial for the charge transport and collection in the device.[4,49,52] However, the PM7(ClCl = 0.2):P(SBDT-ClCl):BTP-eC9

ternary blend film exhibited a larger R_q than that of the PM7(ClCl = 0.2):BTP-eC9 binary blend film. Although a high R_q is observed compared with the PM7(ClCl = 0.2):BTP-eC9 film, the PM7(ClCl = 0.2):P(SBDT-ClCl):BTP-eC9-based film exhibits a favorable morphology for exciton transportation because of the interpenetrating donor−acceptor networks with distinct phase separation.[3,4,26] These results correspond well with the PL and SCLC parameters of the photovoltaic devices.

2.7. Crystallinity and Miscibility Analysis. To obtain an in-depth understanding of the molecular packing and crystalline properties of the pristine terpolymers and optimized terpolymer blend films, 2D-GIWAXS measurements were conducted as displayed in Figure 4.[3,4,20,35,54−56] The corresponding line-cut profiles in the OOP along q_z and in-plane (IP; along q_{xy}) directions and intensity-integrated azimuthal pole figure plots in the (100) scattering peaks were obtained for all films (Figure 5). Specifically, the integrated areas within the azimuthal angle in the range 0−45° (A_z) and 45−90° (A_{xy}) are defined as the corresponding fractions of face-on and edge-on structures, respectively, and the face-on to edge-on structure ratio (A_{xy}/A_z) was also calculated. Finally, the (100) and (010) crystal coherence lengths (CCL$_{(100)}$ and CCL$_{(010)}$) in the OOP direction were calculated from the full width at half-maximum (FWHM) value using the Scherrer equation. The detailed parameters are summarized in Table 4.

First, for the pristine films of bihalogenated thiophene-based terpolymers, the PM7(ClCl = 0.2), PM7(ClBr = 0.2), and PM7(BrBr = 0.2) films exhibited pronounced (010) π−π stacking peaks at q_z = 1.629−1.647 Å^{-1} in the OOP and stronger (100) lamellar stacking peaks at q_{xy} = 0.280−0.293 Å^{-1} in the IP, respectively, which revealed a face-on preferential orientation. The detailed investigation of the
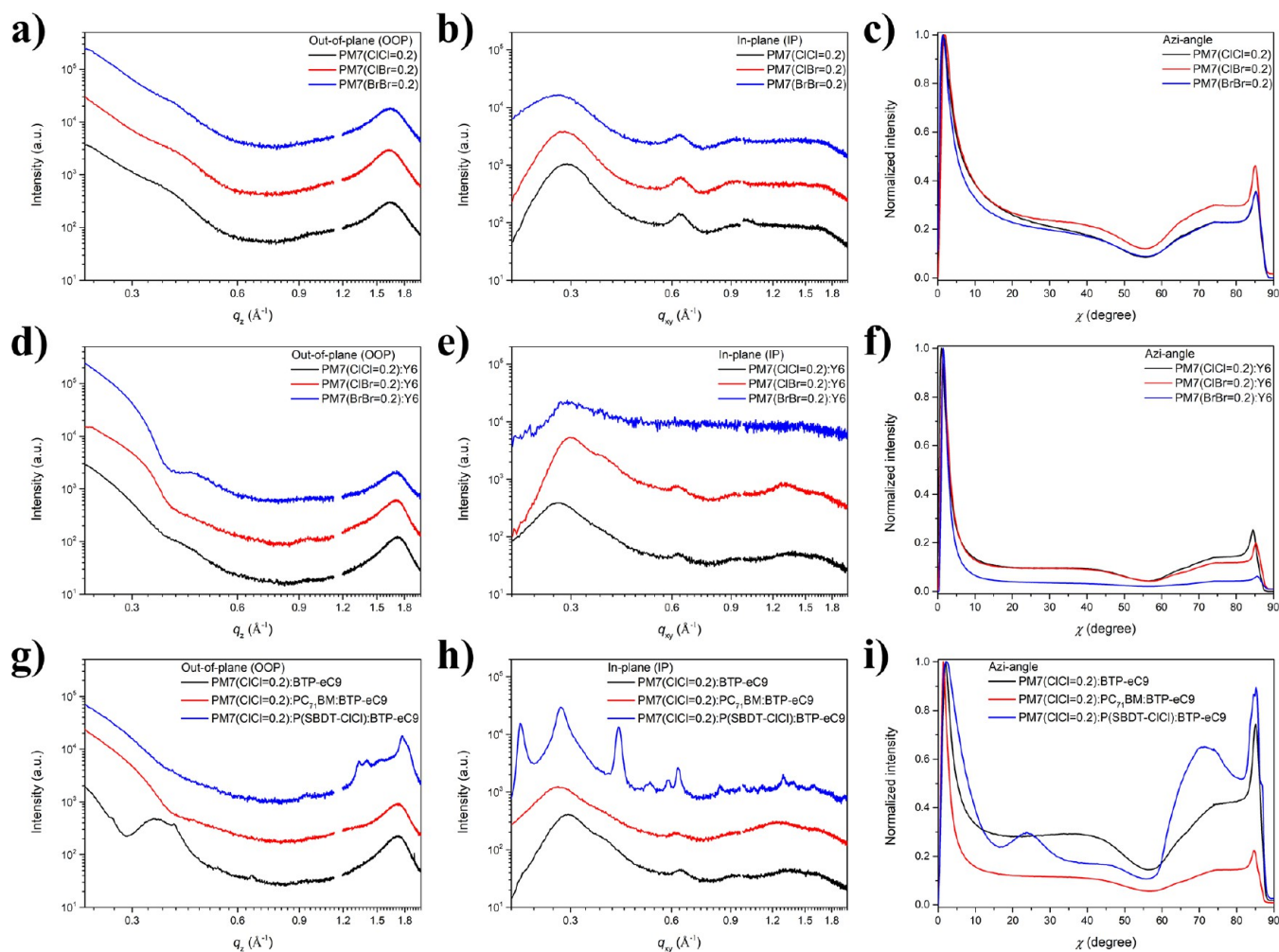
Figure 5. Scattering profiles of the (a–c) neat terpolymers and (d–i) optimized terpolymer blend/ternary blend films: line-cut profiles in (a, d, g) out-of-plane (OOP) and (b, e, h) in-plane (IP) directions and (c, f, i) integrated pole figures from the (100) lamellar diffraction.

Table 4. 2D-GIWAXS Results of the Neat Terpolymer, Terpolymer Blend, and Ternary Blend Films in In-Plane (IP) and Out-of-Plane (OOP) Directions

| terpolymer/terpolymer blend/ternary blend films | IP | | | OOP | | | |
	$d_{(100)}$ [Å] at (100) [Å^{-1}]	FWHM(100)^b [Å^{-1}]	CCL$_{(100)}$^{c} [Å]	$d_{(010)}$ [Å] at (010) [Å^{-1}]	FWHM(010)^b [Å^{-1}]	CCL$_{(010)}$^{c} [Å]	A_{xy}/A_z^{d}
PM7(ClCl = 0.2)	21.44 at 0.293	0.080	70.47	3.81 at 1.647	0.281	20.16	0.52
PM7(ClBr = 0.2)	21.89 at 0.287	0.081	69.97	3.86 at 1.629	0.279	20.30	0.66
PM7(BrBr = 0.2)	22.46 at 0.280	0.108	52.24	3.85 at 1.634	0.288	19.63	0.57
PM7(ClCl = 0.2):Y6	22.61 at 0.278	0.085	66.85	3.65 at 1.720	0.241	23.49	0.59
PM7(ClBr = 0.2):Y6	20.95 at 0.300	0.076	74.75	3.70 at 1.700	0.250	22.59	0.54
PM7(BrBr = 0.2):Y6	21.48 at 0.293	0.207	27.38	3.67 at 1.711	0.288	19.61	0.35
PM7(ClCl = 0.2):BTP-eC9	21.21 at 0.296	0.066	85.07	3.64 at 1.725	0.228	24.84	0.86
PM7(ClCl = 0.2):PC$_{71}$BM:BTP-eC9	22.76 at 0.276	0.082	68.86	3.66 at 1.719	0.276	20.46	0.58
PM7(ClCl = 0.2):P(SBDT-ClCl):BTP-eC9	22.46 at 0.280	0.026	216.08	3.55 at 1.769	0.112	50.39	1.18

$^a q_{xy} = \frac{2\pi}{d_{(100)}}$, $q_z = \frac{2\pi}{d_{(010)}}$. ^{b}FWHM ($\Delta q$) is the full width at half-maximum of the corresponding peaks. ^{c}CCL$_{(100 \text{ or } 010)}$ (Scherrer equation: CCL = $2\frac{\pi K}{\text{FWHM}}$, where K is a shape factor, 0.9) is the crystal coherence length (CCL) of the corresponding crystallite. ^{d}Ratio of the face-on to edge-on orientation determined by the pole figure analysis, where A_{xy} and A_z correspond to the face-on and edge-on fractions, respectively.

face-on to edge-on structure ratio for terpolymers and the A_{xy}/A_z ratios of PM7(ClCl = 0.2), PM7(ClBr = 0.2), and PM7(BrBr = 0.2) exhibited a 0.52, 0.66, and 0.57 in sequence. Despite the limited proportion of face-on structures, the PM7(ClCl = 0.2) film simultaneously exhibited the shortest

π–π ($d_{(010)}$; 3.81 Å) and lamellar stacking ($d_{(100)}$; 21.44 Å) distances, especially the highest CCL$_{(100)}$ of 70.47 Å, which implied that a dense interchain packing was formed because of the dominant crystalline nature of the polymer.[29,56] Furthermore, the trend of molecular stacking and crystalline

properties for terpolymers exhibited a trend similar to the result of the preceding study for bihalogenated thiophene-based D−A polymers. Notably, PM7(BrBr = 0.2) introduced a terpolymer strategy and exhibited a remarkable change in the lamellar ordering with the improved $d_{(100)}$ and $CCL_{(100)}$ compared with that of P(BrBr).

Next, all blend films of the terpolymers based on Y6 exhibited improved $\pi-\pi$ stacking peaks at $q_z = 1.700-1.720$ Å^{-1} by introducing Y6 with an intense face-on structure compared with each binary blend film. Among the terpolymer and Y6 blend films, the PM7(ClCl = 0.2):Y6 blend film exhibited the tightest $d_{(010)}$ with 3.65 Å, and PM7(ClBr = 0.2):Y6 revealed a shortest $d_{(100)}$ with 20.95 Å, which is beneficial to intermolecular charge transport in the vertical and horizontal directions, respectively.[3,4,54,55] In addition, the intensities of $\pi-\pi$ stacking scattering peaks become weaker from PM7(ClCl = 0.2), PM7(ClBr = 0.2), and PM7(BrBr = 0.2)-based blend films. These results are consistent with the trend of CCL change in each direction; in the OOP, $CCL_{(010)}$ = 23.49, 22.59, and 19.61 Å; in the IP, $CCL_{(100)}$ = 66.85, 74.75, and 27.38 Å. For the PM7(BrBr = 0.2):Y6 blend film, lamellar stacking was also depressed along with the decrement of the $\pi-\pi$ stacking effect, which reduced charge transport properties.[29] More importantly, the face-on to edge-on structure ratios of PM7(ClCl = 0.2):Y6, PM7(ClBr = 0.2):Y6, and PM7(BrBr = 0.2):Y6 revealed A_{xy}/A_z values of 0.59, 0.54, and 0.35, respectively, which may be derived from the miscibility between the donor and acceptor.[42,52,55] Among the terpolymer blends with Y6, only PM7(ClCl = 0.2) maintained the face-on structures compared with the pristine terpolymers and rather improved the A_{xy}/A_z ratio from 0.52 to 0.59. These results are consistent with the photovoltaic performance of the fabricated devices.

On introducing BTP-eC9 into the efficient PM7(ClCl = 0.2) instead of Y6, the higher crystalline structures were obtained in both the (010) and (100) orientations; in the OOP, $d_{(010)}$ = 3.64 Å and $CCL_{(010)}$ = 24.84 Å; in the IP, $d_{(100)}$ = 21.21 Å and $CCL_{(100)}$ = 85.07 Å. The improved lamellar packing and preferential face-on structures (A_{xy}/A_z = 0.86) of PM7(ClCl = 0.2):BTP-eC9 resulted in enhanced photovoltaic performance and especially a high FF derived from a distinct lamellar structure located at q_z = 0.347 Å^{-1} in the OOP.[44,57] For the ternary blend incorporated PC$_{71}$BM on PM7(ClCl = 0.2):BTP-eC9, the crystalline properties in both OOP and IP directions decreased and resulted in poor performance. The other ternary blend, PM7(ClCl = 0.2):P(SBDT-ClCl):BTP-eC9-based film exhibited a dominant face-on orientation (A_{xy}/A_z = 1.18) despite the introduction of P(SBDT-ClCl) with high crystallinity.[42,44] Notably, a tight $\pi-\pi$ stacking peak was observed at q_z = 1.769 Å^{-1}. At around the main $\pi-\pi$ stacking peak in the OOP, even big and small multiple diffraction signals (q_z of 1.539, 1.401, and 1.332 Å^{-1}) were observed, which supported the charge transport properties.[58,59] Moreover, the IP for the PM7(ClCl = 0.2):P(SBDT-ClCl):BTP-eC9 ternary blend film also revealed similar phenomena, that is, three distinct ordered structures located at q_{xy} of 0.212, 0.280, and 0.416 Å^{-1} displayed with packing distances of 29.64, 22.44, and 15.10 Å. Furthermore, the PM7(ClCl = 0.2):P(SBDT-ClCl):BTP-eC9 ternary blend film exhibited the largest $CCL_{(100)}$ and $CCL_{(010)}$ (216.08 and 50.39 Å) among the fabricated devices, which revealed that the extremely strong crystallinity may result in high photovoltaic performance.[44,58,59]

The 2D-GIWAXS results revealed that the inherent crystallinity of the bihalogenated thiophene-based terpolymers changed after mixing with Y6 derivatives. The phenomenon may be related to the compatibility of the donor and acceptor. Therefore, the phase separation between the donor and acceptor was analyzed to understand the miscibility of active layer materials used in this study.[19,36,42,46,52,54,55,60] The surface tensions (γ) of each material were evaluated according to the Wu model from the contact angle measurement of two solvents (water and diiodomethane (DIM)) on the neat films (Figure S30). First, three terpolymers of PM7(ClCl = 0.2), PM7(ClBr = 0.2), and PM7(BrBr = 0.2) exhibited gradually decreasing water contact angles of 103.5, 102.7, and 102.2° and the same trend was observed for DIM contact angles with 48.0, 47.5, and 45.5° in sequence. Therefore, the γ values were 35.93, 36.21, and 37.04 mN m^{-1}, respectively. From the contact angle data and the corresponding γ values, an estimation of the miscibility for donor and acceptor blends was performed using the Flory−Huggins interaction parameter (χ) based on the surface tension data using the equation suggested by Moon.[46,60] Therefore, the calculated χ values of PM7(ClCl = 0.2):Y6, PM7(ClBr = 0.2):Y6, and PM7(BrBr = 0.2):Y6 were 0.15, 0.13, and 0.09, respectively. These values implied that χ parameters decrease from PM7(ClCl = 0.2) to PM7(BrBr = 0.2) in sequence, which resulted in the enhanced miscibility with Y6 along with the increment of the bihalogen atomic size, which reduces domain purity gradually in the active layer. The smallest χ value for the PM7(BrBr = 0.2):Y6 blend indicated excessive miscibility and poor domain purity, which could influence the charge transport and phase separation, resulting in the lowest PCE.[35,46,54,55,60]

Comparison of the miscibility of PM7(ClCl = 0.2) with the BTP-eC9 acceptor instead of Y6 revealed higher χ parameters of 0.29, 0.36, and 0.31 for the PM7(ClCl = 0.2):BTP-eC9, PM7(ClCl = 0.2):PC$_{71}$BM:BTP-eC9, and PM7(ClCl = 0.2):P(SBDT-ClCl):BTP-eC9 systems, respectively. These values implied that the three blends based on BTP-eC9 exhibited low miscibility and high domain purity and efficient phase separation. As mentioned in the aforementioned correlation between photovoltaic performance and crystallinity, all χ parameters except for PM7(ClCl = 0.2):PC$_{71}$BM:BTP-eC9 were consistent with PCE and crystallinity trends in this study.[46,54,55,60] PM7(ClCl = 0.2):PC$_{71}$BM:BTP-eC9 revealed that the biggest χ value leads to the lowest miscibility among the blends and a less homogeneous morphology, which hinders charge transfer and exciton dissociation at the donor/acceptor interface. Based on these results and the comprehensive analysis of crystallinity and miscibility between terpolymer blends based on Y6, PM7(ClCl = 0.2) still maintains excellent crystallinity after mixing with Y6 to improve the phase separation, whereas PM7(ClBr = 0.2) and PM7(BrBr = 0.2)-based blends exhibit lower face-on structures. In our case, balanced miscibility and high crystallinity were realized in PM7(ClCl = 0.2):P(SBDT-ClCl):BTP-eC9, and the result is consistent with the aforementioned photovoltaic performance, morphology, and charge transport properties. The detailed parameters are summarized in Table S16.

2.8. Potential in PM7(ClCl = 0.2)-Based Semitransparent Organic Solar Cells. To further investigate the scalability of efficient OSCs, we tested batch-to-batch variation of PM7(ClCl = 0.2) with diverse molecular weights. As presented in Table S17, three batches of PM7(ClCl = 0.2) with M_n and PDI variation from 28.9 kDa (M: moderate), 49.9 kDa (H:
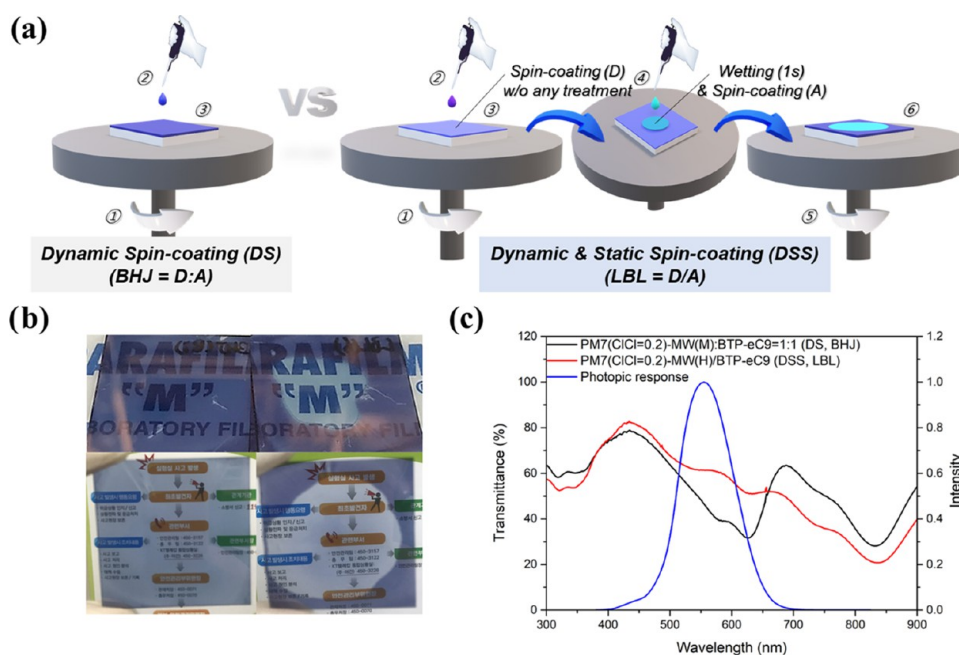
Figure 6. (a) Spin-coating process of the bulk-heterojunction (BHJ) and layer-by-layer (LBL) films using dynamic spin-coating (DS) and dynamic and static spin-coating (DSS), (b) photographs and (c) transmittance spectra of the optimized PM7(ClCl = 0.2)-MW(M):BTP-eC9 = 1:1 (DS, BHJ) and PM7(ClCl = 0.2)-MW(H)/BTP-eC9 (DSS, LBL) films.

high), and 75.5 kDa (VH: very high) and PDI 1.25, 1.28, and 1.32 revealed the best efficiency of 14.5−15.2% with a variation smaller than 4.6%, which indicated excellent batch-to-batch reproducibility and high solubility in the eco-friendly solvent, XY. To understand the photovoltaic performance concerning molecular weight, the UV−Vis absorption spectra of the three batches of PM7(ClCl = 0.2)-MW(M/H/VH) were acquired to assess the inherent aggregation behaviors. As displayed in Figure S31, the three thin films exhibited distinct aggregation patterns. Upon comparing a relative interchain packing, the 0−0/0−1 ratio from the normalized spectra for PM7(ClCl = 0.2)-MW(M/H/VH), revealed a 1.09, 1.07, and 1.06, respectively, in sequence. Furthermore, based on the aggregation properties of PM7(ClCl = 0.2)-MW(M), a dominated J-aggregation and H-aggregation were observed in PM7(ClCl = 0.2)-MW(H) and PM7(ClCl = 0.2)-MW(VH), respectively, which is consistent with the trend of J_{sc} and FF of the photovoltaic results.

To extend the practicability of PM7(ClCl = 0.2), the LBL approach enabling control of the morphology and vertical phase separation was introduced to fabricate semitransparent organic solar cells (ST-OSCs).[61−65] Notably, the PM7(ClCl = 0.2)-MW(M) film was almost washed away after the CF coating relative to the initial film. Such a phenomenon is unusual because of the processing of most donor polymers (e.g., PM6) with similar molecular weight properties using a sequential LBL (Figure S32).[62,63] Herein, we newly suggest that the LBL strategy based on this unique polymer feature is a promising technique for reaching highly transparent ST-OSCs. Given the aforementioned issue, controlling the solution concentration and spin rates of PM7(ClCl = 0.2) concerning the molecular weight is critical for ensuring device performance reproducibility in LBL processing. To effectively optimize the performance of the LBL-based device, the absorption profiles for the PM7(ClCl = 0.2)-MW(H/VH) neat films according to the CF coating with various additives were investigated, and

three of each were selected as a promising additive combination (Figure S33). Thus, the absorption films of PM7(ClCl = 0.2)-MW(H) changed considerably after the CF coating than those of PM7(ClCl = 0.2)-MW(VH), which indicated that the additive exhibits a pronounced difference for J-aggregates and the 0−0/0−1 ratio. The thickness of PM7(ClCl = 0.2)-MW(M/H/VH) and BTP-eC9 was carefully investigated, and the PM7(ClCl = 0.2)-MW(H)/BTP-eC9 film achieved a maximum PCE of 13.1% with a high average visible transmittance (AVT, @ 380−780 nm) of 60.8% (only active layer film) among the LBL-processed opaque devices of three batches for PM7(ClCl = 0.2). These properties are desirable for achieving high performance and transmittance for use in ST-OSCs. The detailed optimizing procedures for LBL-processed devices are summarized in Tables S18−20.

As displayed in Figure 6a, unlike the DS method used in the BHJ-based process, the highly reproducible DSS method was introduced with a two-step LBL process involving sequential deposition of donor and acceptor layers. In this strategy, the acceptor solution is applied to the preformed donor film and spin-coated after wetting for 1 s. This wetting time can generate high reproducibility for film thickness and uniformity. The detailed photovoltaic parameters with respect to the wetting time are summarized in Table S21, and the processing video is provided for better understanding in the Supporting Information. The optimized films of PM7(ClCl = 0.2)-MW(M):BTP-eC9 (DS, BHJ) and PM7(ClCl = 0.2)-MW-(H)/BTP-eC9 (DSS, LBL) were systematically studied and directly compared for both opaque and semitransparent devices. Figure 6b,c details drastically different films in terms of transparency, which can highlight that an AVT of 60.8% for the optimal LBL film is considerably larger than 46.6%. Furthermore, relative photopic transmittance (T; @ 550 nm) and color rendering index (CRI) perceived by human eyes were calculated with 47.1% and 77.9 for the BHJ-processed film, 61.4% and 79.0 for the LBL-processed film, respectively.
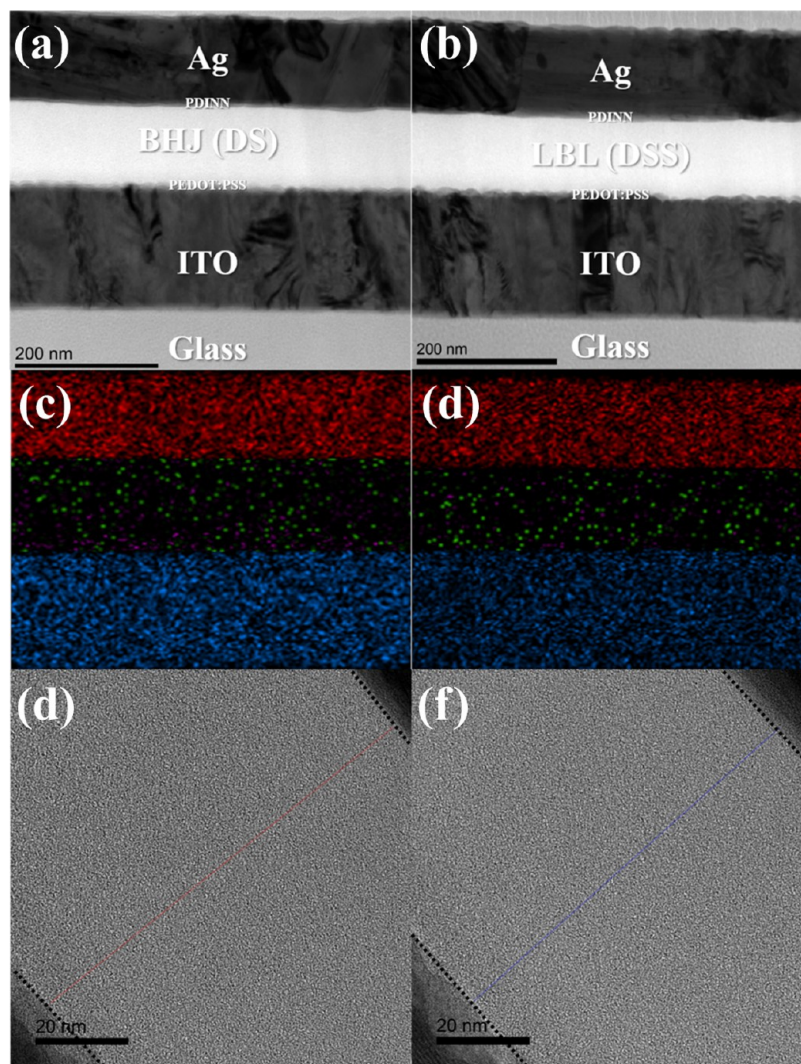
Figure 7. Cross-sectional TEM images of the optimized (a, c, e) PM7(ClCl = 0.2)-MW(M):BTP-eC9 = 1:1 (DS, BHJ) and (b, d, f) PM7(ClCl = 0.2)-MW(H)/BTP-eC9 (DSS, LBL) devices: cross-sectional TEM images (200 nm scale), overlapped EDS mapping (200 nm scale) with Ag (red), Cl (green), N (violet), and In (blue), and zoomed-in cross-sectional TEM images (20 nm scale) of both opaque OSC devices.

Their color coordinates (x, y) were also plotted in the Commission Internationale de l'Eclairage (CIE) 1931 chromaticity diagram (Figure S34), which indicated that LBL-processed ST-OSCs could be tuned to increase the transparency and neutral color with a larger AVT, T, and CRI than BHJ-based devices.

To investigate the mechanism of the LBL and DSS techniques to achieve favorable results for reasonable performance and transmittance simultaneously, AFM and high resolution-transmission electron microscopy (HR-TEM) measurements were conducted.[5,14,15,27,53,56,65] As displayed in Figure S35, both pure PM7(ClCl = 0.2)-MW(H) and -MW(VH) films exhibited a fibrillar feature that is associated with material self-aggregation with a large R_q of 6.08 and 6.89 nm, respectively. After introducing CF (0.25% 1,8-diiodooctane, DIO) into each PM7(ClCl = 0.2) film, the more drastically varied surface morphology of PM7(ClCl)-MW(H) indicates that a solvent considerably affects the oversized aggregation of the polymer compared with that of PM7(ClCl)-MW(VH). Neat PM7(ClCl)-MW(H) films generated the nanosized aggregation, which enabled continuous phase segregation with a reduced R_q of 4.53 nm for processing of

BTP-eC9 dissolved in the corresponding solvent. As displayed in Figure S36, such a distinct change can be observed in TEM images compared with PM7(ClCl = 0.2)-MW(M):BTP-eC9 (DS, BHJ) and PM7(ClCl = 0.2)-MW(H)/BTP-eC9 (DSS, LBL) films. A network of fibrils with defined phase separation is visible in the LBL-processed film. The introduction of the polymer with a high molecular weight ensured that the enhanced crystalline structure facilitated the bicontinuous donor—acceptor networks, which enabled efficient charge transport with similar nanosized domains such as the BHJ-processed film.[27,56]

Scanning vertical and cross-sectional TEM analysis with energy-dispersive (EDS) mapping was performed to investigate the difference between BHJ and LBL-based blend morphologies.[5,14,15,65] As displayed in Figure S37, the results of carbon (C) mapping for both scanning TEM films revealed dense intermixing with high coverage between donor and acceptor components. Because nitrogen (N) only exists in BTP-eC9, it was used as an elemental indicator to investigate the distribution and position of the acceptor in each film. The results revealed that the LBL-based film had more N than the BHJ-based film, whereas the Cl signal was weak. Thus, the

donor content decreased in the corresponding film area because of LBL processing with the DSS method. Furthermore, cross-sectional TEM with EDS mapping in Figure 7 revealed that the configuration of each device exhibited a distinct active layer thickness (Figure S38) and distribution of the donor and acceptor. The optimized thickness of BHJ and LBL-processed films was estimated at 95−100 and 85−90 nm, respectively, using the scale bar from each TEM image. However, we could not discern notable differences in the donor and acceptor distribution from the bright field. The results of stacked N and Cl mapping indicated that the LBL-processed film was beneficial for charge separation and transport compared to that observed for the distribution of the BHJ-processed film. Crucially, the LBL-processed film revealed that the BTP-eC9 network penetrated the network of PM7(ClCl = 0.2)-MW(H) and widely spread the whole region without leaning in the region close to the bottom of the film, which facilitated favorable photocurrent generation and transport in the vertical phase. Although the thickness showed less than 85−90 nm, the efficiency of LBL processing was comparable to the BHJ-processed film.[62,63,65] The detailed data for the aforementioned charge transport properties are summarized through PL and SCLC in Figure S39 and Table S22.

To investigate the origin of the suppressed charge recombination in the LBL-based film, we investigated the nanostructural crystallinity and domain properties through 2D-GIWAXS and 2D small-angle X-ray scattering (2D-GISAXS).[36,39,46,54,55,59,64−66] Figures S40 and S41 display the 2D scattering patterns and 1D line-cut profiles for 2D-GIWAXS. The peak-fitting analysis was conducted, and the corresponding data are displayed in Table S23. In short, for the LBL-based film, both $d_{(010)}$ and $CCL_{(010)}$ slightly decreased, whereas $d_{(100)}$ and $CCL_{(100)}$ increased, especially, $CCL_{(100)}$ largely changed from 85.07 to 129.88 Å compared with that of the BHJ-based film. This phenomenon resulted in improved charge transport in the vertical direction.[61,63] Next, the 2D-GISAXS patterns and the corresponding intensities along the IP direction of each thin film are displayed in Figures S42 and S43. The Debye−Anderson−Brumberger (DAB) and fractal core−shell models were used to analyze the scattering contribution from intermixing amorphous phases and acceptor domains, respectively.[39,66] As presented in Table S24, the BTP-eC9 domain size $(2R_g)$ of the LBL-based film (52.89 nm) is smaller than that of the BHJ-based film (54.53 nm), which is in accordance with the slightly decreased face-on orientation with a relatively low $CCL_{(100)}$ as presented in 2D-GIWAXS. By contrast, the correlation length (ξ) of the intermixing phases for the LBL-based film increased to 40.40 from 30.51 nm of the BHJ-based film, which revealed that donor packing was tight and required pronounced phase separation (i.e., the high molecular weight of PM7(ClCl = 0.2) exhibits multilength-scale structures with a large domain size).[39,65] The suitable difference between the donor and acceptor domains is beneficial for charge transport in the active layer.[66] This result is consistent with the 2D-GIWAXS and TEM results of the corresponding device conditions.

We used time-resolved photoluminescence (TRPL) to estimate the lifetime of the photon-generated charge carriers and correlate the nanostructural properties with the exciton dissociation for BHJ and LBL-based films.[16,26,40,54,58,64] Figure S44 displays the normalized TRPL curves obtained for both films. The excited lifetime can reveal the energy-transfer process within the active layer. Generally, a lower lifetime indicates an efficient energy-transfer process in the active layer.[16,58] The detailed calculation method is displayed in the Supporting Information. Table S25 lists the fitted lifetime parameters. Both the BHJ and LBL-based films exhibited fast charge dissociation with similar average-decay lifetimes (τ_{ave}) of 0.159 and 0.192 ns, respectively, which indicated that although the donor content largely decreases, the LBL-based film exhibits an efficient hole transfer process, which verified the similarly high exciton dissociation efficiency with the BHJ-based film, as discussed previously. Comprehensively, the LBL process with the DSS method based on PM7(ClCl = 0.2)-MW(H) allows precise adjustment of the crystallinity and orientation to promote nanostructure formation with proper domain sizes in a less thin film.

The aforementioned studies revealed that PM7(ClCl = 0.2)-MW(H)/BTP-eC9 exhibits considerable potential in ST-OSCs. By the unique LBL process using the DSS method, we achieved superior ST-OSCs compared with that of PM7(ClCl = 0.2)-MW(M):BTP-eC9 with the BHJ structure. The 15 nm Ag electrode was used for fabricating ST-OSCs because of its balance between the transmittance and sheet resistance, which can generally form a stable and uniform film structure, and thus ensure excellent transmittance with reduced electrical resistance.[32,65,67] The detailed photovoltaic parameters of the optimized opaque and semitransparent devices are summarized in Figures S45 and S46 and Table 5. Both BHJ and LBL-based ST-OSCs revealed an overall decreased J_{sc} compared with their opaque counterparts. Importantly, the complementary absorption between the donor and acceptor was maintained even in the LBL-processed structure. As a result, the LBL-processed ST-OSC simultaneously exhibited a high PCE and AVT with 11.5 and 27.1%, which are more reasonable than those of the BHJ-based ST-OSC with 12.9 and 18.0%, respectively. In addition, LBL-processed ST-OSCs show reliability and an overall smaller deviation of an average PCE compared with that of BHJ-based ST-OSCs, indicating excellent reproducibility. More importantly, although the donor content decreased, LBL-processed ST-OSC retained 87.8% efficiency compared with that of the opaque device, whereas BHJ-based ST-OSC retained 84.9% of its initial efficiency. Therefore, LBL-based ST-OSC exhibited a higher LUE of 3.06% than that of BHJ-based ST-OSC (2.32%). The difference between both ST-OSCs can be discriminated with the corresponding transmittance spectra, EQE curves, and photographs as displayed in Figure 8.

To improve the transmittance and simultaneously maintain PCE, tungsten trioxide (WO_3) was designed as a DBR to optimize the optical interference in the UV−Vis range.[68] Because this layer was introduced with 30 nm, a high PCE of 10.8% can be achieved with the considerably enhanced AVT of 33.4% (T = 33.9% @550 nm). The detailed data are displayed in Figure S47. In particular, the transmittance increased considerably with a combination of Ag and WO_3 in the range of the visible region of 380−780 nm, containing the most sensitive wavelength for human eyes that view in the range 400−700 nm. The EQE exhibited the corresponding weak wavelength dependence. Furthermore, PCE and AVT, CIE 1931 color space, CRI, and correlated color temperature (CCT) were used to evaluate the performance of the LBL-processed ST-OSCs with a combination of Ag and WO_3 under an AM 1.5G illumination light source. The color coordinates were (0.273, 0.285), and the correlative CRI and CCT were

Table 5. Photovoltaic Performance of the Optimized Devices (Opaque/Semitransparent) for PM7(ClCl = 0.2)-MW(M):BTP-eC9 = 1:1 (DS, BHJ) and PM7(ClCl = 0.2)-MW(H)/BTP-eC9 (DSS, LBL)

active layer	coating method	top electrode	V_{oc} [V]	J_{sc} [mA cm^{-2}]	FF [%]	PCE$_{max}$/PCE$_{ave}^a$ [%]	AVT^b [eV]	LUE^c [eV]
PM7(ClCl = 0.2)-MW(M):BTP-eC9 = 1.0:1.0 (BHJ)	DS	Ag (100 nm)	0.879	24.21	71.63	15.2/15.1 ± 0.14	46.6^d	
	DS	Ag (15 nm)	0.879	20.95	68.11	12.9/12.6 ± 0.26	18.0	2.32
PM7(ClCl = 0.2)-MW(H)/BTP-eC9 (LBL)	DSS	Ag (100 nm)	0.879	22.33	66.80	13.1/12.9 ± 0.19	60.8^d	
	DSS	Ag (15 nm)	0.858	20.43	65.52	11.5/11.3 ± 0.22	27.1	3.12
	DSS	Ag (15 nm)/WO$_3$ (30 nm)	0.858	19.51	64.54	10.8/10.6 ± 0.23	33.4	3.61
			0.850	20.925	62.742	11.157^e		3.73

^{a}Average PCE values calculated from 10 independent cells. ^{b}Average visible transmittance (AVT) calculated from the whole visible region (380–780 nm). ^{c}Light utilization efficiency (LUE; LUE = PCE × AVT) is proposed to judge the ST-OSCs. ^{d}Only active layer film's AVT. ^{e}Certification result from the Nano Convergence Practical Application Center (NCPAC), Republic of Korea (No. TP-21S-0062).

74.48 and 10,927 K, respectively, which indicated that the ST-OSCs with a combination of Ag and WO$_3$ exhibited a clear sky-blue characteristic. The high transparency of ST-OSC ensures clear visualization, as displayed in Figure S48. Because of the stable ST-OSC with a combination of Ag and WO$_3$, we could evaluate the cell performance after encapsulation from the NCPAC, Republic of Korea. A PCE of 11.157% (No. TP-21S-0062) was recorded, which, to the best of our knowledge, is the first certified ST-OSC with a high LUE of 3.73% (Figure S49).[32,65,67,69] These results highlight the advantage of the novel dichlorinated thiophene-based terpolymer and LBL-process strategy in the development and application of ST-OSCs.

3. CONCLUSIONS

Three wide-band-gap donor terpolymers, namely, PM7(ClCl = 0.2), PM7(ClBr = 0.2), and PM7(BrBr = 0.2) were synthesized by introducing bihalogenated thiophenes with a 20% concentration as a third component instead of the BDD unit in the main backbone of PM7. This terpolymer strategy based on Cl-2DBDT obtained with a relatively low cost compared to F-2DBDT showed a simple and cost-effective method for improving their optical and electrochemical properties, solubility, and crystallinity which can realize high photovoltaic performances. The resulting terpolymers exhibited high yields of more than 85% and excellent solubility in eco-friendly solvents such as TL and XL. Among the terpolymers, PM7(ClCl = 0.2)-based devices with the BHJ exhibited the highest potential for photovoltaic performance with a PCE of 15.2% despite using TL. Furthermore, the PM7(ClCl = 0.2)-based ternary blend device achieved the best PCE of 15.8% using the newly synthesized high-crystallinity polymer, P(SBDT-ClCl). As further work, highly efficient semitransparent OSCs (ST-OSCs) were fabricated by combining LBL and sequential DSS techniques according to the molecular weight of PM7(ClCl = 0.2)-MW(M/H/VH). The AVT of active layer films can be markedly enhanced from 46.6% to 60.8% with visible absorbing donor contents decreasing from BHJ to LBL. Using this unique LBL strategy, the PM7(ClCl = 0.2)-MW(H)-processed ST-OSCs yield a high PCE of 11.5% with an AVT of 27.1% with outstanding tolerance to device reproducibility. By optimizing ST-OSCs with WO$_3$ as a DBR, a considerable LUE of 3.61% was realized with a PCE of 10.8% and an AVT of 33.4% (certified PCE ≈ 11.157%; LUE ≈ 3.73%). This study provides novel perspectives for developing efficient and feasible photoactive materials for commercializing NFOSCs.

4. EXPERIMENTAL SECTION

4.1. Polymerization of PM7(ClCl = 0.2). A mixture of Cl-2DBDT (194.7 mg, 0.20 mmol), BDD (122.7 mg, 0.16 mmol), ClCl (12.4 mg, 0.04 mmol), and Pd(pph$_3$)$_4$ (7.0 mg) was added to a microwave-assisted 10–20 mL vial in an air environment. The vial was capped and evacuated for 20 min before it was refilled with nitrogen gas, after which anhydrous toluene (5.0 mL) was added to the mixture. The reactor was twice degassed and refilled with nitrogen. The polymerization mixture was stirred at 100 °C for 8 h. The polymer was end-capped by the addition of 2-bromothiophene (112.0 mg, 0.66 mmol), and the mixture was further heated at 110 °C for 1 h. After heating, 2-tributylstannyl thiophene (62.6 mg, 0.175 mmol) was added, and the mixture was heated again at 110 °C for 1 h. The reaction mixture was cooled to room temperature and poured into methanol (300 mL) and 37% HCl (10 mL), stirred for 1 h and subsequently purified using a Soxhlet extractor with methanol (24 h),
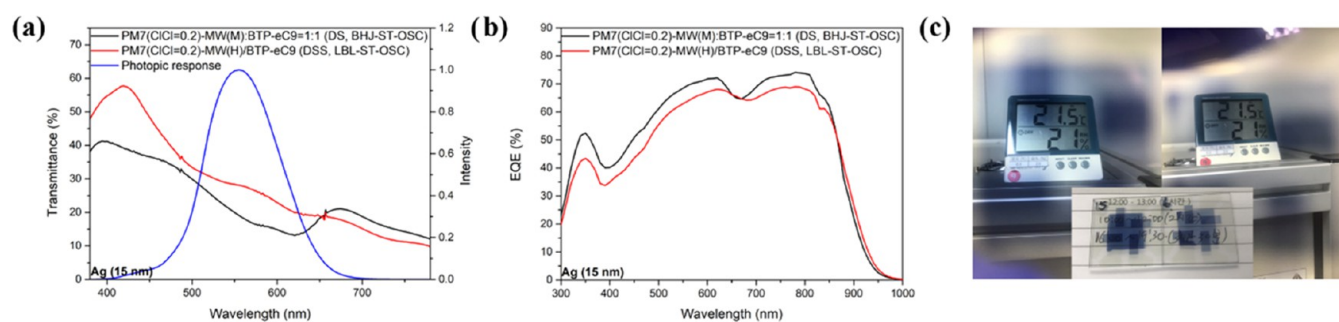
Figure 8. (a) Transmittance spectra, (b) EQE curves, and (c) photographs of the optimized semitransparent devices for PM7(ClCl = 0.2)-MW(M):BTP-eC9 = 1:1 (DS, BHJ) and PM7(ClCl = 0.2)-MW(H)/BTP-eC9 (DSS, LBL).

acetone (24 h), hexane (24 h), methylene chloride (24 h), and chloroform (24 h), sequentially. The chloroform fraction of the polymer was reprecipitated in methanol, filtered, and vacuum dried to obtain PM7(ClCl = 0.2) (dark blue-black solid; yield: 91.0%). PM7(ClBr = 0.2) (dark blue solid; yield: 87.5%) and PM7(BrBr = 0.2) (dark violet solid; yield: 85.0%) were synthesized under the same conditions and procedures.

■ ASSOCIATED CONTENT

Ⓢ Supporting Information

The Supporting Information is available free of charge at https://pubs.acs.org/doi/10.1021/acsami.2c10286.

Sources of all reagents and chemicals used in this study; information of instruments and characterization methods; fabrication and characterization conditions of organic solar cells for all synthesized polymers/terpolymers (with ternary blends); the details of AVT calculations; the details of SCLC and TRPL measurements; supplementary notes for synthesizing monomers and polymers/terpolymers (with ternary blends) with data of ^{1}H/^{13}C NMR, GC-MS, and DFT calculations (dihedral angles, simulated HOMO, LUMO, and band gap energy levels); GPC (molecular weights and polydispersity indices); TGA (decomposition temperatures); DSC, UV−Vis (optical band gaps); CV (HOMO/LUMO energy levels); 2D-GIWAXS (lamellar and π−π stacking distances, FWHMs, coherence lengths, and the face-on to edge-on structure ratio)/GISAXS (domain sizes); photovoltaic parameters with J−V and EQE; SCLC (charge carrier mobilities and electron and hole balance); PL (photoluminescence quenching efficiencies); contact angle measurement (surface tension energies and Flory−Huggins interaction parameters); AFM (topography and phase images with root-mean-square roughness values); HR-TEM/cross-sectional TEM with EDS mapping; TRPL (exciton lifetimes); and CIE data, photograph, and the PCE certificate of the optimized semitransparent organic solar cells (PDF)

Video S1 (MP4)

■ AUTHOR INFORMATION

Corresponding Author

Doo Kyung Moon − *Nano and Information Materials (NIMs) Laboratory, Department of Chemical Engineering, Konkuk University, Seoul 05029, Korea;* ⓘ orcid.org/0000-0001-9482-7508; Email: dkmoon@konkuk.ac.kr

Authors

Sung Jae Jeon − *Nano and Information Materials (NIMs) Laboratory, Department of Chemical Engineering, Konkuk University, Seoul 05029, Korea*

Nam Gyu Yang − *Nano and Information Materials (NIMs) Laboratory, Department of Chemical Engineering, Konkuk University, Seoul 05029, Korea*

Young Hoon Kim − *Nano and Information Materials (NIMs) Laboratory, Department of Chemical Engineering, Konkuk University, Seoul 05029, Korea*

Ji Hee Yun − *Nano and Information Materials (NIMs) Laboratory, Department of Chemical Engineering, Konkuk University, Seoul 05029, Korea*

Complete contact information is available at:
https://pubs.acs.org/10.1021/acsami.2c10286

Notes

The authors declare no competing financial interest.

■ REFERENCES

(1) Meng, L.; Zhang, Y.; Wan, X.; Li, C.; Zhang, X.; Wang, Y.; Ke, X.; Xiao, Z.; Ding, L.; Xia, R.; Yip, H. L.; Cao, Y.; Chen, Y. Organic and Solution-Processed Tandem Solar Cells With 17.3% Efficiency. *Science* **2018**, *361*, 1094−1098.

(2) Yuan, J.; Zhang, Y.; Zhou, L.; Zhang, G.; Yip, H. L.; Lau, T. K.; Lu, X.; Zhu, C.; Peng, H.; Johnson, P. A.; Leclerc, M.; Cao, Y.; Ulanski, J.; Li, Y.; Zou, Y. Single-Junction Organic Solar Cell with Over 15% Efficiency Using Fused-Ring Acceptor with Electron-Deficient Core. *Joule* **2019**, *3*, 1140−1151.

(3) Li, C.; Zhou, J.; Song, J.; Xu, J.; Zhang, H.; Zhang, X.; Guo, J.; Zhu, L.; Wei, D.; Han, G.; Min, J.; Zhang, Y.; Xie, Z.; Yi, Y.; Yan, H.; Gao, F.; Liu, F.; Sun, Y. Non-Fullerene Acceptors with Branched Side Chains and Improved Molecular Packing to Exceed 18% Efficiency in Organic Solar Cells. *Nat. Energy* **2021**, *6*, 605−613.

(4) Cui, Y.; Yao, H.; Zhang, J.; Xian, K.; Zhang, T.; Hong, L.; Wang, Y.; Xu, Y.; Ma, K.; An, C.; He, C.; Wei, Z.; Gao, F.; Hou, J. Single-Junction Organic Photovoltaic Cells with Approaching 18% Efficiency. *Adv. Mater.* **2020**, *32*, No. 1908205.

(5) Zheng, Z.; Wang, J.; Bi, P.; Ren, J.; Wang, Y.; Yang, Y.; Liu, X.; Zhang, S.; Hou, J. Industrial Viability of Single-Component Organic Solar Cells. *Joule* **2022**, *6*, 171.

(6) Xu, C.; Jin, K.; Xiao, Z.; Zhao, Z.; Ma, X.; Wang, X.; Li, J.; Xu, W.; Zhang, S.; Ding, L.; Zhang, F. Wide Bandgap Polymer with Narrow Photon Harvesting in Visible Light Range Enables Efficient Semitransparent Organic Photovoltaics. *Adv. Funct. Mater.* **2021**, *31*, No. 2107934.

(7) Xu, C.; Jin, K.; Xiao, Z.; Zhao, Z.; Yan, Y.; Zhu, X.; Li, X.; Zhou, Z.; Jeong, S. Y.; Ding, L.; Woo, H. Y.; Yuan, G.; Zhang, F. Efficient Semitransparent Layer-by-Layer Organic Photovoltaics via Optimizing Wide Bandgap and Narrow Absorption Polymer Layer Thickness. *Sol. RRL* **2022**, *6*, No. 2200308.

(8) Hu, Z.; Wang, J.; Wang, Z.; Gao, W.; An, Q.; Zhang, M.; Ma, X.; Wang, J.; Miao, J.; Yang, C.; Zhang, F. Semitransparent Ternary Nonfullerene Polymer Solar Cells Exhibiting 9.40% Efficiency and 24.6% Average Visible Transmittance. *Nano Energy* **2019**, *55*, 424−432.

(9) Hu, Z.; Wang, J.; Ma, X.; Gao, J.; Xu, C.; Wang, X.; Zhang, X.; Wang, Z.; Zhang, F. Semitransparent Organic Solar Cells Exhibiting 13.02% Efficiency and 20.2% Average Visible Transmittance. *J. Mater. Chem. A* **2021**, *9*, 6797−6804.

(10) Hu, Z.; Wang, Z.; An, Q.; Zhang, F. Semitransparent Polymer Solar Cells with 12.37% Efficiency and 18.6% Average Visible Transmittance. *Sci. Bull.* **2020**, *65*, 131−137.

(11) Zhang, Y.; Luo, D.; Shan, C.; Liu, Q.; Gu, X.; Li, W.; Choy, W. C. H.; Kyaw, A. K. K. High-Performance Semitransparent Organic Solar Cells Enabled by Improved Charge Transport and Optical Engineering of Ternary Blend Active Layer. *Sol. RRL* **2022**, *6*, No. 2100785.

(12) Xie, Y.; Cai, Y.; Zhu, L.; Xia, R.; Ye, L.; Feng, X.; Yip, H. L.; Liu, F.; Lu, G.; Tan, S.; Sun, Y. Fibril Network Strategy Enables High-Performance Semitransparent Organic Solar Cells. *Adv. Funct. Mater.* **2020**, *30*, No. 2002181.

(13) Xue, R.; Zhang, J.; Li, Y.; Li, Y. Organic Solar Cell Materials Toward Commercialization. *Small* **2018**, *14*, No. 1801793.

(14) Jeon, S. J.; Han, Y. W.; Moon, D. K. Chlorine Effects of Heterocyclic Ring-Based Donor Polymer for Low-Cost and High-Performance Nonfullerene Polymer Solar Cells. *Sol. RRL* **2019**, *3*, No. 1900094.

(15) Sun, C.; Pan, F.; Bin, H.; Zhang, J.; Xue, L.; Qiu, B.; Wei, Z.; Zhang, Z. G.; Li, Y. A Low Cost and High Performance Polymer Donor Material for Polymer Solar Cells. *Nat. Commun.* **2018**, *9*, No. 743.

(16) Ren, J.; Bi, P.; Zhang, J.; Liu, J.; Wang, J.; Xu, Y.; Wei, Z.; Zhang, S.; Hou, J. Molecular Design Revitalizes the Low-Cost PTV-Polymer for Highly Efficient Organic Solar Cells. *Natl. Sci. Rev.* **2021**, *8*, No. nwab031.

(17) Cheng, P.; Zhan, X. Stability of Organic Solar Cells: Challenges and Strategies. *Chem. Soc. Rev.* **2016**, *45*, 2544−2582.

(18) Ghasemi, M.; Balar, N.; Peng, Z.; Hu, H.; Qin, Y.; Kim, T.; Rech, J. J.; Bidwell, M.; Mask, W.; McCulloch, I.; You, W.; Amassian, A.; Risko, C.; O'Connor, B. T.; Ade, H. A Molecular Interaction−Diffusion Framework for Predicting Organic Solar Cell Stability. *Nat. Mater.* **2021**, *20*, 525.

(19) Han, Y. W.; Jeon, S. J.; Lee, H. S.; Park, H.; Kim, K. S.; Lee, H. W.; Moon, D. K. Evaporation-Free Nonfullerene Flexible Organic Solar Cell Modules Manufactured by an All-Solution Process. *Adv. Energy Mater.* **2019**, *9*, No. 1902065.

(20) Jeon, S. J.; Han, Y. W.; Moon, D. K. 13.9%-Efficiency and Eco-Friendly Nonfullerene Polymer Solar Cells Obtained by Balancing Molecular Weight and Solubility in Chlorinated Thiophene-Based Polymer Backbones. *Small* **2019**, *15*, No. 1902598.

(21) Li, S.; Li, C.-Z.; Shi, M.; Chen, H. New Phase for Organic Solar Cell Research: Emergence of Y-Series Electron Acceptors and Their Perspectives. *ACS Energy Lett.* **2020**, *5*, 1554−1567.

(22) Liu, Q.; Jiang, Y.; Jin, K.; Qin, J.; Xu, J.; Li, W.; Xiong, J.; Liu, J.; Xiao, Z.; Sun, K.; Yang, S.; Zhang, X.; Ding, L. 18% Efficiency Organic Solar Cells. *Sci. Bull.* **2020**, *65*, 272−275.

(23) Ying, L.; Huang, F.; Bazan, G. C. Regioregular Narrow-Bandgap-Conjugated Polymers for Plastic Electronics. *Nat. Commun.* **2017**, *8*, No. 14047.

(24) Wang, H.; Lu, H.; Chen, Y. N.; Ran, G.; Zhang, A.; Li, D.; Yu, N.; Zhang, Z.; Liu, Y.; Xu, X.; Zhang, W.; Bao, Q.; Tang, Z.; Bo, Z. Chlorination Enabling a Low-Cost Benzodithiophene-Based Wide-Bandgap Donor Polymer with an Efficiency of over 17%. *Adv. Mater.* **2022**, *34*, No. 2105483.

(25) Wu, J.; Li, G.; Fang, J.; Guo, X.; Zhu, L.; Guo, B.; Wang, Y.; Zhang, G.; Arunagiri, L.; Liu, F.; Yan, H.; Zhang, M.; Li, Y. Random Terpolymer Based on Thiophene-Thiazolothiazole Unit Enabling Efficient Non-Fullerene Organic Solar Cells. *Nat. Commun.* **2020**, *11*, No. 4612.

(26) An, Q.; Wang, J.; Ma, X.; Gao, J.; Hu, Z.; Liu, B.; Sun, H.; Guo, X.; Zhang, X.; Zhang, F. Two Compatible Polymer Donors Contribute Synergistically for Ternary Organic Solar Cells With 17.53% Efficiency. *Energy Environ. Sci.* **2020**, *13*, 5039−5047.

(27) Song, J.; Ye, L.; Li, C.; Xu, J.; Chandrabose, S.; Weng, K.; Cai, Y.; Xie, Y.; O'Reilly, P.; Chen, K.; Zhou, J.; Zhou, Y.; Hodgkiss, J. M.; Liu, F.; Sun, Y. An Optimized Fibril Network Morphology Enables High-Efficiency and Ambient-Stable Polymer Solar Cells. *Adv. Sci.* **2020**, *7*, No. 2001986.

(28) Yuan, J.; Ford, M. J.; Zhang, Y.; Dong, H.; Li, Z.; Li, Y.; Nguyen, T. Q.; Bazan, G. C.; Ma, W. Toward Thermal Stable and High Photovoltaic Efficiency Ternary Conjugated Copolymers: Influence of Backbone Fluorination and Regioselectivity. *Chem. Mater.* **2017**, *29*, 1758−1768.

(29) Sun, C.; Pan, F.; Chen, S.; Wang, R.; Sun, R.; Shang, Z.; Qiu, B.; Min, J.; Lv, M.; Meng, L.; Zhang, C.; Xiao, M.; Yang, C.; Li, Y. Achieving Fast Charge Separation and Low Nonradiative Recombination Loss by Rational Fluorination for High-Efficiency Polymer Solar Cells. *Adv. Mater.* **2019**, *31*, No. 1905480.

(30) Zhang, S.; Qin, Y.; Zhu, J.; Hou, J. Over 14% Efficiency in Polymer Solar Cells Enabled by a Chlorinated Polymer Donor. *Adv. Mater.* **2018**, *30*, No. 1800868.

(31) Jeon, S. J.; Kim, Y. H.; Hong, D. H.; Yang, N. G.; Han, Y. W.; Moon, D. K. Molecular Design of Efficient Chlorine- and Carboxylate-Functionalized Donor Polymers for Nonfullerene Organic Solar Cells Enabling Processing with Eco-Friendly Solvent in Air. *Sol. RRL* **2020**, *5*, No. 2000608.

(32) Wang, H.; Lu, H.; Chen, Y. N.; Zhang, A.; Liu, Y.; Li, D.; Liu, Y.; Xu, X.; Bo, Z. A Versatile Planar Building Block with C2V Symmetry for High-Performance Non-Halogenated Solvent Processable Polymer Donors. *Adv. Energy Mater.* **2022**, *12*, No. 2104028.

(33) Wu, Y.; An, C.; Shi, L.; Yang, L.; Qin, Y.; Liang, N.; He, C.; Wang, Z.; Hou, J. The Crucial Role of Chlorinated Thiophene Orientation in Conjugated Polymers for Photovoltaic Devices. *Angew. Chem., Int. Ed.* **2018**, *57*, 12911−12915.

(34) Po, R.; Bianchi, G.; Carbonera, C.; Pellegrino, A. "All That Glisters Is Not Gold": An Analysis of the Synthetic Complexity of Efficient Polymer Donors for Polymer Solar Cells. *Macromolecules* **2015**, *48*, 453−461.

(35) Kini, G. P.; Jeon, S. J.; Moon, D. K. Design Principles and Synergistic Effects of Chlorination on a Conjugated Backbone for Efficient Organic Photovoltaics: A Critical Review. *Adv. Mater.* **2020**, *32*, No. 1906175.

(36) Wan, S. S.; Xu, X.; Jiang, Z.; Yuan, J.; Mahmood, A.; Yuan, G. Z.; Liu, K. K.; Ma, W.; Peng, Q.; Wang, J. L. A Bromine and Chlorine Concurrently Functionalized End Group for Benzo[1,2-b:4,5-b′]-diselenophene-Based Nonfluorinated Acceptors: New Hybrid Strategy to Balance the Crystallinity and Miscibility of Blend Films Enabling Highly Efficient Polymer Solar Cells. *J. Mater. Chem. A* **2020**, *8*, 4856−4867.

(37) Cui, Y.; Zhu, P.; Liao, X.; Chen, Y. Recent Advances of Computational Chemistry in Organic Solar Cell Research. *J. Mater. Chem. C* **2020**, *8*, 15920−15939.

(38) Ye, L.; Li, W.; Guo, X.; Zhang, M.; Ade, H. Polymer Side-Chain Variation Induces Microstructural Disparity in Nonfullerene Solar Cells. *Chem. Mater.* **2019**, *31*, 6568−6577.

(39) Li, W.; Chen, M.; Cai, J.; Spooner, E. L. K.; Zhang, H.; Gurney, R. S.; Liu, D.; Xiao, Z.; Lidzey, D. G.; Ding, L.; Wang, T. Molecular

Order Control of Non-fullerene Acceptors for High-Efficiency Polymer Solar Cells. *Joule* 2019, 3, 819−833.

(40) Li, S.; Zhan, L.; Sun, C.; Zhu, H.; Zhou, G.; Yang, W.; Shi, M.; Li, C. Z.; Hou, J.; Li, Y.; Chen, H. Highly Efficient Fullerene-Free Organic Solar Cells Operate at Near Zero Highest Occupied Molecular Orbital Offsets. *J. Am. Chem. Soc.* 2019, 141, 3073−3082.

(41) Sun, C.; Qin, S.; Wang, R.; Chen, S.; Pan, F.; Qiu, B.; Shang, Z.; Meng, L.; Zhang, C.; Xiao, M.; Yang, C.; Li, Y. High Efficiency Polymer Solar Cells with Efficient Hole Transfer at Zero Highest Occupied Molecular Orbital Offset between Methylated Polymer Donor and Brominated Acceptor. *J. Am. Chem. Soc.* 2020, 142, 1465−1474.

(42) Naveed, H. B.; Ma, W. Miscibility-Driven Optimization of Nanostructures in Ternary Organic Solar Cells Using Non-fullerene Acceptors. *Joule* 2018, 2, 621.

(43) Peng, Z.; Jiang, K.; Qin, Y.; Li, M.; Balar, N.; O'Connor, B. T.; Ade, H.; Ye, L.; Geng, Y. Modulation of Morphological, Mechanical, and Photovoltaic Properties of Ternary Organic Photovoltaic Blends for Optimum Operation. *Adv. Energy Mater.* 2021, 11, No. 2003506.

(44) Chen, Z.; Song, W.; Yu, K.; Ge, J.; Zhang, J.; Xie, L.; Peng, R.; Ge, Z. Small-Molecule Donor Guest Achieves Rigid 18.5% and Flexible 15.9% Efficiency Organic Photovoltaic Via Fine-Tuning Microstructure Morphology. *Joule* 2021, 5, 2395−2407.

(45) Lee, S.; Jeong, D.; Kim, C.; Lee, C.; Kang, H.; Woo, H. Y.; Kim, B. J. Eco-Friendly Polymer Solar Cells: Advances in Green-Solvent Processing and Material Design. *ACS Nano* 2020, 14, 14493−14527.

(46) Wu, J.; Liao, C. Y.; Chen, Y.; Jacobberger, R. M.; Huang, W.; Zheng, D.; Tsai, K. W.; Li, W. L.; Lu, Z.; Huang, Y.; Wasielewski, M. R.; Chang, Y. M.; Marks, T. J.; Facchetti, A. To Fluorinate or Not to Fluorinate in Organic Solar Cells: Achieving a Higher PCE of 15.2% when the Donor Polymer is Halogen-Free. *Adv. Energy Mater.* 2021, 11, No. 2102648.

(47) Fan, B.; Lin, F.; Oh, J.; Fu, H.; Gao, W.; Fan, Q.; Zhu, Z.; Li, W. J.; Li, N.; Ying, L.; Huang, F.; Yang, C.; Jen, A. K. Y. Enabling High Efficiency of Hydrocarbon-Solvent Processed Organic Solar Cells through Balanced Charge Generation and Non-Radiative Loss. *Adv. Energy Mater.* 2021, 11, No. 2101768.

(48) Zhang, J.; Liu, W.; Zhou, G.; Yi, Y.; Xu, S.; Liu, F.; Zhu, H.; Zhu, X. Accurate Determination of the Minimum HOMO Offset for Efficient Charge Generation using Organic Semiconducting Alloys. *Adv. Energy Mater.* 2020, 10, No. 1903298.

(49) Jeon, S. J.; Kim, Y. H.; Kim, I. N.; Yang, N. G.; Yun, J. H.; Moon, D. K. Utilizing 3,4-Ethylenedioxythiophene (EDOT)-Bridged Non-Fullerene Acceptors for Efficient Organic Solar Cells. *J. Energy Chem.* 2022, 65, 194−204.

(50) Yu, J. E.; Jeon, S. J.; Choi, J. Y.; Han, Y. W.; Ko, E. J.; Moon, D. K. A 3-Fluoro-4-hexylthiophene-Based Wide Bandgap Donor Polymer for 10.9% Efficiency Eco-Friendly Nonfullerene Organic Solar Cells. *Small* 2019, 15, No. 1805321.

(51) Chao, P.; Chen, H.; Pu, M.; Zhu, Y.; Han, L.; Zheng, N.; Zhou, J.; Chang, X.; Mo, D.; Xie, Z.; Meng, H.; He, F. Chlorinated Benzo[1,2-b:4,5-c']dithiophene-4,8-dione Polymer Donor: A Small Atom Makes a Big Difference. *Adv. Sci.* 2021, 8, No. 2003641.

(52) Jeon, S. J.; Han, Y. W.; Kim, Y. H.; Moon, D. K. Case Study on the Correlation between Crystal Packing and Miscibility of Chlorinated Thiophene−Based Donor Polymers for Nonfullerene Organic Solar Cells with Long Shelf Life. *Sol. RRL* 2020, 4, No. 2000074.

(53) Zhu, L.; Zhang, M.; Zhong, W.; Leng, S.; Zhou, G.; Zou, Y.; Su, X.; Ding, H.; Gu, P.; Liu, F.; Zhang, Y. Progress and Prospects of the Morphology of Non-Fullerene Acceptor Based High-Efficiency Organic Solar Cells. *Energy Environ. Sci.* 2021, 14, 4341−4357.

(54) Zhang, L.; Xu, X.; Lin, B.; Zhao, H.; Li, T.; Xin, J.; Bi, Z.; Qiu, G.; Guo, S.; Zhou, K.; Zhan, X.; Ma, W. Achieving Balanced Crystallinity of Donor and Acceptor by Combining Blade-Coating and Ternary Strategies in Organic Solar Cells. *Adv. Mater.* 2018, 30, No. 1805041.

(55) Li, Y.; Zheng, N.; Yu, L.; Wen, S.; Gao, C.; Sun, M.; Yang, R. A Simple Phenyl Group Introduced at the Tail of Alkyl Side Chains of

Small Molecular Acceptors: New Strategy to Balance the Crystallinity of Acceptors and Miscibility of Bulk Heterojunction Enabling Highly Efficient Organic Solar Cells. *Adv. Mater.* 2019, 31, No. 1807832.

(56) Weng, K.; Ye, L.; Zhu, L.; Xu, J.; Zhou, J.; Feng, X.; Lu, G.; Tan, S.; Liu, F.; Sun, Y. Optimized Active Layer Morphology Toward Efficient and Polymer Batch Insensitive Organic Solar Cells. *Nat. Commun.* 2020, 11, No. 2855.

(57) Gao, W.; Liu, T.; Zhong, C.; Zhang, G.; Zhang, Y.; Ming, R.; Zhang, L.; Xin, J.; Wu, K.; Guo, Y.; Ma, W.; Yan, H.; Liu, Y.; Yang, C. Asymmetrical Small Molecule Acceptor Enabling Nonfullerene Polymer Solar Cell with Fill Factor Approaching 79%. *ACS Energy Lett.* 2018, 3, 1760−1768.

(58) Dong, X.; Yang, K.; Tang, H.; Hu, D.; Chen, S.; Zhang, J.; Kan, Z.; Duan, T.; Hu, C.; Dai, X.; Xiao, Z.; Sun, K.; Lu, S. Improving Molecular Planarity by Changing Alky Chain Position Enables 12.3% Efficiency All-Small-Molecule Organic Solar Cells with Enhanced Carrier Lifetime and Reduced Recombination. *Sol. RRL* 2019, 4, No. 1900326.

(59) Ye, L.; Weng, K.; Xu, J.; Du, X.; Chandrabose, S.; Chen, K.; Zhou, J.; Han, G.; Tan, S.; Xie, Z.; Yi, Y.; Li, N.; Liu, F.; Hodgkiss, J. M.; Brabec, C. J.; Sun, Y. Unravelling the Influence of Non-Fullerene Acceptor Molecular Packing on Photovoltaic Performance of Organic Solar Cells. *Nat. Commun.* 2020, 11, No. 6005.

(60) Xue, X.; Weng, K.; Qi, F.; Zhang, Y.; Wang, Z.; Ali, J.; Wei, D.; Sun, Y.; Liu, F.; Wan, M.; Liu, J.; Huo, L. Steric Engineering of Alkylthiolation Side Chains to Finely Tune Miscibility in Non-fullerene Polymer Solar Cells. *Adv. Energy Mater.* 2019, 9, No. 1802686.

(61) Xu, X.; Yu, L.; Meng, H.; Dai, L.; Yan, H.; Li, R.; Peng, Q. Polymer Solar Cells with 18.74% Efficiency: From Bulk Heterojunction to Interdigitated Bulk Heterojunction. *Adv. Funct. Mater.* 2022, 32, No. 2108797.

(62) Ning, H.; Jiang, Q.; Han, P.; Lin, M.; Zhang, G.; Chen, J.; Chen, H.; Zeng, S.; Gao, J.; Liu, J.; He, F.; Wu, Q. Manipulating the Solubility Properties of Polymer Donors for High-Performance Layer-by-Layer Processed Organic Solar Cells. *Energy Environ. Sci.* 2021, 14, 5919−5928.

(63) Fu, H.; Gao, W.; Li, Y.; Lin, F.; Wu, X.; Son, J. H.; Luo, J.; Woo, H. Y.; Zhu, Z.; Jen, A. K. Y. A Generally Applicable Approach Using Sequential Deposition to Enable Highly Efficient Organic Solar Cells. *Small Methods* 2020, 4, No. 2000687.

(64) Li, Q.; Wang, L. M.; Liu, S.; Guo, L.; Dong, S.; Ma, G.; Cao, Z.; Zhan, X.; Gu, X.; Zhu, T.; Cai, Y. P.; Huang, F. Vertical Composition Distribution and Crystallinity Regulations Enable High-Performance Polymer Solar Cells with >17% Efficiency. *ACS Energy Lett.* 2020, 5, 3637−3646.

(65) Wang, H. C.; Cheng, P.; Tan, S.; Chen, C. H.; Chang, B.; Tsao, C. S.; Chen, L. Y.; Hsieh, C. A.; Lin, Y. C.; Cheng, H. W.; Yang, Y.; Wei, K. H. Sequential Deposition of Donor and Acceptor Provides High-Performance Semitransparent Organic Photovoltaics Having a Pseudo p−i−n Active Layer Structure. *Adv. Energy Mater.* 2021, 11, No. 2003576.

(66) Mahmood, A.; Wang, J. L. A Review of Grazing Incidence Small- and Wide-Angle X-Ray Scattering Techniques for Exploring the Film Morphology of Organic Solar Cells. *Sol. RRL* 2020, 4, No. 2000337.

(67) Yin, P.; Yin, Z.; Ma, Y.; Zheng, Q. Improving the Charge Transport of the Ternary Blend Active Layer for Efficient Semi-transparent Organic Solar Cells. *Energy Environ. Sci.* 2020, 13, 5177−5185.

(68) Chen, C.-Y.; Tan, G.-H.; Hsu, H.-L.; Chen, C.-P.; Lin, H.-W. Recent Progress on Advanced Optical Structures for Emerging Photovoltaics and Photodetectors. *Adv. Energy Sustainability Res.* 2020, 1, No. 2000035.

(69) Kini, G. P.; Jeon, S. J.; Moon, D. K. Latest Progress on Photoabsorbent Materials for Multifunctional Semitransparent Organic Solar Cells. *Adv. Funct. Mater.* 2021, 31, No. 2007931.